



## Millennial-scale carbon accumulation and molecular transformation in a permafrost core from Interior Alaska

J.A. Hutchings<sup>a,\*</sup>, T.S. Bianchi<sup>a</sup>, D.S. Kaufman<sup>c</sup>, A.L. Kholodov<sup>d</sup>, D.R. Vaughn<sup>a</sup>,  
E.A.G. Schuur<sup>b</sup>

<sup>a</sup> Department of Geological Sciences, University of Florida, Gainesville, FL, USA

<sup>b</sup> Center for Ecosystem Science and Society, Northern Arizona University, Flagstaff, AZ, USA

<sup>c</sup> School of Earth and Sustainability, Northern Arizona University, Flagstaff, AZ, USA

<sup>d</sup> Geophysical Institute, University of Alaska Fairbanks, Fairbanks, AK, USA

Received 27 September 2018; accepted in revised form 23 March 2019; available online 1 April 2019

### Abstract

Organic carbon stored in high-latitude permafrost represents a potential positive feedback to climate warming as well as a valuable store of paleoenvironmental information. The below-freezing conditions have effectively removed permafrost organic material from the modern carbon cycle and preserved its pre-freezing bulk and molecular states. The conditions that lead to efficient burial of organic carbon (OC) within permafrost were investigated by measuring OC stocks, past accumulation rates, and biogeochemical composition of a permafrost core taken from Interior Alaska dating back to 40 ka. The post-glacial Marine Isotope Stage 1 is represented by the top 1.2 m of the core and contains 64.7 kg OC/m<sup>2</sup> with an accumulation rate of 4.3 g OC/m<sup>2</sup>/yr. The sediments that accumulated around the Last Glacial Maximum contain 9.9 kg OC/m<sup>2</sup> with an accumulation rate of 0.5 g OC/m<sup>2</sup>/yr. Carbon storage (144.7 kg OC/m<sup>2</sup>) and accumulation (26.1 g OC/m<sup>2</sup>/yr) are both observed to be greatest between 35 and 40 ka, late during the Marine Isotope Stage 3 global interstadial. The extent of OC degradation was assessed using lignin and amino acid biomarkers with both approaches indicating well-preserved contemporary active layer and interstadial OC, whereas stadial OC was highly degraded. Lignin compositional indices throughout the core appear altered by sorptive processes that confounded some expected trends in the overall organic matter composition, while amino acids provided a more integrated pattern of change. Significant correlations between carbon-normalized hydroxyproline and total lignin concentrations further support the usefulness of hydroxyproline as an indicator for the abundance of plant organic matter. A novel amino acid plant-microbial index of the ratio of microbial-specific muramic acid and diaminopimelic acid biomarkers to the plant-specific hydroxyproline biomarker, indicate a transition from plant-dominated organic matter in fresh organic soils (index values of 0.01–0.20) to more microbial-dominated organic matter in degraded mineral soils (index values of 0.50–2.50). The branched glycerol dialkyl glycerol tetraether composition is complex and is not immediately compatible with existing temperature transfer functions. Residence time within the active layer is interpreted to integrate key factors such as primary productivity, inorganic sediment delivery, and other climate factors that control soil organic matter degradation. The Marine Isotope Stage 3, mid-Wisconsin interstadial period at this locality was forest-dominated and suggests the currently prevailing tundra ecotone is sensitive to environmental change. The majority of buried permafrost OC is high in degradability and if thawed, would be expected to be highly vulnerable to microbial decomposition.

© 2019 Elsevier Ltd. All rights reserved.

\* Corresponding author at: Department of Earth and Planetary Sciences, Washington University, St. Louis, MO, USA.  
E-mail address: [jackh@wustl.edu](mailto:jackh@wustl.edu) (J.A. Hutchings).

**Keywords:** organic carbon; permafrost; biomarkers; lignin phenols; amino acids; branched GDGTs

## 1. INTRODUCTION

The northern circumpolar region stores high soil organic carbon (OC) stocks compared to lower latitudes as a consequence of slow rates of decomposition under cold climate conditions, as well as storage at perennially subzero temperatures within permafrost (Zimov et al., 2006; Schuur et al., 2008). This disparity is threatened under current and future climate warming scenarios, wherein the rate of decomposition in surface soils is enhanced and frozen permafrost carbon is thawed and remineralized (Schuur et al., 2015). Current coverage of permafrost-affected landscape is greatly reduced compared to its most recent maximum extent during the Last Glacial Maximum (LGM, ca. 20 ka ago), and projections for the balance of this century and beyond indicate even greater reductions (Lawrence and Slater, 2005; Lindgren et al., 2016). The relative size of the northern circumpolar carbon stock (1330–1580 Pg C) to the carbon dioxide (CO<sub>2</sub>) stock of the atmosphere (~859 Pg C), combined with the vulnerability of permafrost-affected terrain to warming, reinforces the global relevance of the fate of these frozen soils and sediments (Hugelius et al., 2014; Dlugokencky and Tans, 2017). Recent modeling of permafrost-climate interactions indicates that 246–436 Pg C will thaw and be susceptible to remineralization processes by the end of this century (Harden et al., 2012).

The majority (~800 Pg C) of circumpolar carbon stocks are located within permafrost that accumulated during the Late Pleistocene and Holocene (Hugelius et al., 2014). The so-called *yedoma* stocks that accumulated in non-glaciated regions of Siberia and Alaska are of biogeochemical interest, as their amount and composition reflects the variable climate states during their deposition, including interstadial events and the deglacial transition into the Holocene (Schirrmeister et al., 2002; Strauss et al., 2017). *Yedoma* sequences are characterized by high ice content, with some regions having more than 80% water content by volume, which may exacerbate their vulnerability to warming because of thermokarst development (Schirrmeister et al., 2011; Kuhry et al., 2013). The paleoenvironmental context of these sequences as well as Holocene-aged permafrost is critical to understanding the conditions under which carbon accumulated, as well as potential post-thaw greenhouse gas emissions (Blinnikov et al., 2011; Wetterich et al., 2011; Vonk et al., 2013; Lapointe et al., 2017).

Molecular biomarkers generated by primary producers and soil microorganisms have been increasingly applied in circumpolar studies owing to their greater specificity of source and degradation state (i.e., apparently quality) of organic matter, compared to bulk indicators (Zech et al., 2010; Philben et al., 2014; Routh et al., 2014; Zhang et al., 2017; Stapel et al., 2018). Lignin, a structural polymer produced by vascular plants, has been used extensively in other ecosystems (see reviews in Thevenot et al., 2010; Jex et al., 2014). The phenolic composition of lignin in a material is indicative of the amount of vascular plant material relative

to other sources, the degradation state of the lignin, as well as the relative types of vascular plant tissue inputs (Hedges and Ertel, 1982; Hedges et al., 1988; Goñi and Hedges, 1995). Free amino acids and oligopeptides in soil solution have been observed to rapidly cycle due to plant uptake (Kielland, 1994; Farrell et al., 2013), whereas soil hydrolyzable amino acids represent a much larger pool that tends to shift in composition from plant-oriented to microbial-oriented with increased degradation (Friedel and Scheller, 2002; Miltner et al., 2009). In addition to overall shifts in composition, secondary, non-proteinogenic amino acid biomarkers synthesized for a variety of purposes, including cellular lipid structure, can provide additional constraints on the source and quality of OC (Philben et al., 2014; Menzel et al., 2015; Philben et al., 2016).

The quality of permafrost organic matter will influence the vulnerability of carbon stocks as high-latitude systems experience climate warming and permafrost thaw. With warming, permafrost can undergo gradual, top-down thaw or rapid destabilization via thermokarst formation (Murton and French, 1993; French and Shur, 2010). Thawed soil may then enter the contemporary carbon cycle through microbial processing, which drives the permafrost carbon feedback, whereby mineralization of stored permafrost organic carbon drives further climate warming. Bulk properties such as C:N have been shown to be able to predict post-thaw carbon emissions, but model fits are still poor and precise predictions of overall post-thaw reactivity are needed (Schädel et al., 2014; Weiss et al., 2016; Faucherre et al., 2018). Molecular biomarkers allow for inference into specific pools of organic carbon and may provide better predictive power on post-thaw reactivity.

There has been extensive work on the paleoecological context of Late Pleistocene deposits in Alaska (Hopkins et al., 1982; Kanevskiy et al., 2011; Lachniet et al., 2012; Schirrmeister et al., 2016; Lapointe et al., 2017). Past studies typically used bulk geochemical and pollen-based indicators, but some have also employed molecular biomarkers to characterize permafrost organic matter and even fewer have used multiple such variables. Here, we present a multi-variable analysis of a permafrost core taken from Interior Alaska that spans from the contemporary active layer to 40 ka, and includes a dated, organic-carbon-rich section deposited during Marine Isotope Stage (MIS) 3. Our objectives were to (1) estimate millennial-scale carbon accumulation rates, (2) characterize the quality of organic matter using lignin and amino acid biomarkers, and (3) examine the relationship between organic matter amount, quality, and paleoenvironmental context.

## 2. MATERIALS AND METHODS

### 2.1. Field site and sampling

The core for this study was collected from the Eight Mile Lake watershed (Fig. 1 63.88°N, 149.25°W) near the town

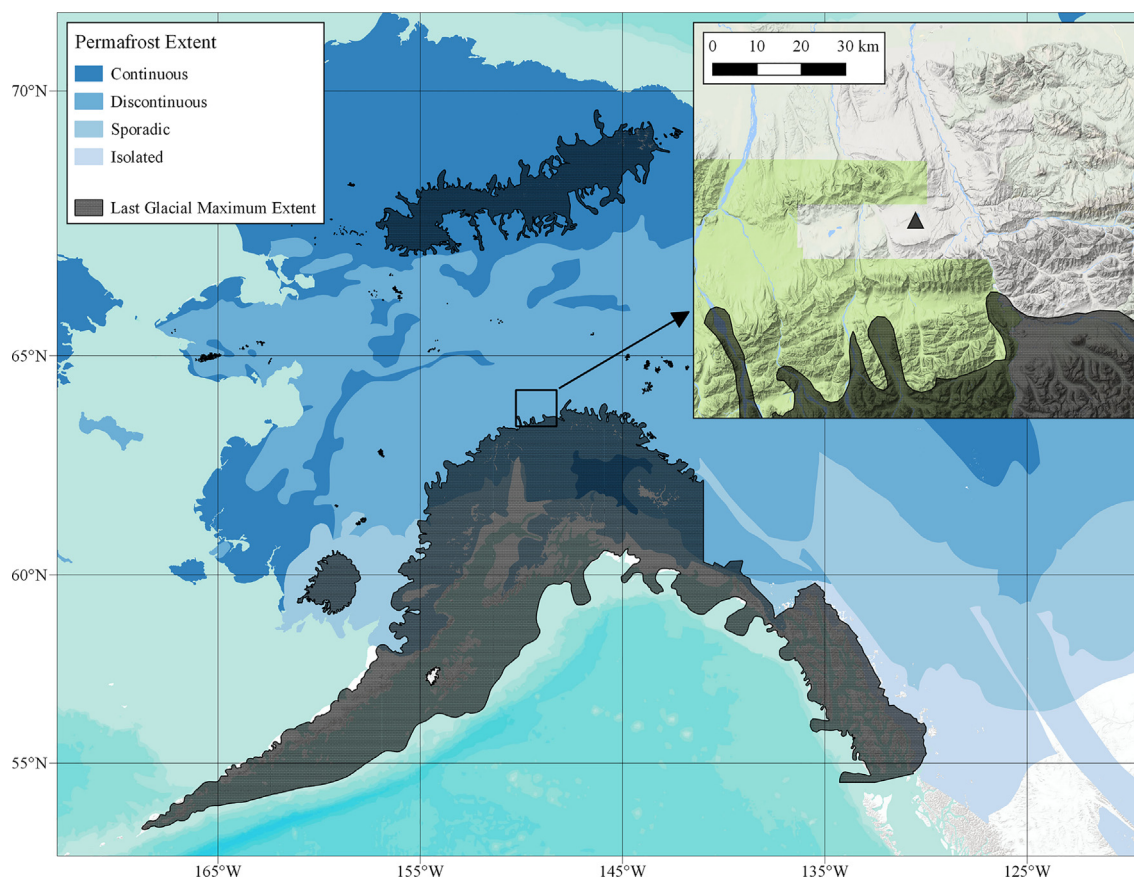


Fig. 1. A map of Alaska shaded with permafrost extent (Brown et al., 1997) and glacial extent during the last glacial maximum (Kaufman and Manley, 2004). The inset shows the location of the Eight Mile Lake locality with Denali National Park shaded in green. (For interpretation of the references to colour in this figure legend, the reader is referred to the web version of this article.)

of Healy in the northern foothills of the Alaska Range. This location is approximately 30 km north of the maximum extent of Alaska range glaciers during the LGM (Fig. 1) and is the site of several ongoing studies that have described the modern carbon cycle and plant community (Vogel et al., 2009; Schuur et al., 2009; Mauritz et al., 2017). The area is characterized as moist, acidic tundra dominated by the tussock-forming sedge *Eriophorum vaginatum*, various small shrubs, and *Sphagnum* spp. mosses (Schuur et al., 2007). Long-term permafrost temperatures at the site have been monitored by a borehole installed in 1985, with permafrost temperatures approximating the mean annual air temperatures at the site of  $-1\text{ }^{\circ}\text{C}$  (Osterkamp and Romanovsky, 1999), and permafrost temperatures have been rising in recent decades (Osterkamp et al., 2009).

A 5.4-m-long permafrost core was extracted in March 2015, using a combination of a hand-held Cold Regions Research Laboratory SIPRE permafrost corer (top 1 m) and a UKB-12/25 coring rig (1–5.4 m, Drilling Technologies Factory, Russia), with coring terminated by an unidentified obstruction. Field work was accomplished while air temperatures were well below  $0\text{ }^{\circ}\text{C}$  and the extracted core was transported frozen to the University of Alaska, Fairbanks for processing. The core was split lengthwise, photographed, and cut into  $\sim 5\text{ cm}$  sections. Split sections of

the core were shipped frozen to Northern Arizona University and University of Florida for further processing.

## 2.2. Bulk biogeochemistry

Bulk density and ice content of core sections were determined by displacement of ethanol in a cold-room and mass difference while frozen (i.e., including ice content) and after oven-drying, yielding wet and dry bulk density values, as well as ice content by volume and mass. The ice content of permafrost soils is indicative of both environmental conditions during accumulation and post-depositional thaw events (French and Shur, 2010).

Core sections were freeze-dried and plant macrofossils were picked for radiocarbon measurement. Dried sections were passed through a 2 mm sieve and then homogenized using a roller-mill, following Arnold and Schepers (2004). All further analyses were performed on the freeze-dried, homogenized core sections. Total carbon and nitrogen were measured on a Carlo Erba NA 1500 CNS Elemental Analyzer. Total inorganic carbon was determined by acidification with phosphoric acid, using an AutoMate Prep Device (Automate FX, USA) coupled to a UIC 5014  $\text{CO}_2$  coulometer. Total organic carbon (TOC) was determined as the difference between total carbon and total inorganic

carbon. The organic carbon (OC) stable isotope ratio ( $\delta^{13}\text{C}$ ) was determined by acidification with 1 N hydrochloric acid (HCl) to remove carbonates, double rinsing with ultrapure water, drying, and analysis by flash combustion on a Carlo Erba NA 1500 CNS Elemental Analyzer coupled to Thermo Electron Delta V Advantage isotope ratio mass spectrometer.

TOC was measured for 49 of 85 (58%) core sections and missing values were estimated by linear interpolation between values in the over- and under-lying measured sections. Gap-filled TOC estimates were only used when estimating OC stocks. TOC was initially sampled every ~20 cm and increased in resolution as needed to further resolve downcore transitions in bulk and molecular indices. OC stocks in units of kg OC/m<sup>2</sup> were determined for each sample as the product of dry bulk density, section length, and TOC.

### 2.3. Radiocarbon dating and age-depth model

Macrofossils were picked, described (Table A1), and subjected to acid-base-acid pretreatment to remove exogenous carbon (Santos and Ormsby, 2013). Radiocarbon samples were prepared for analysis at either the University of Florida or Northern Arizona University. For either laboratory's preparation, macrofossils were converted to CO<sub>2</sub> in evacuated, sealed quartz tubes containing cupric oxide (CuO). Combusted CO<sub>2</sub> at the University of Florida was then purified and reduced to graphite by the sealed-tube Zn-reduction method (Xu et al., 2007) and submitted to the National Ocean Sciences Accelerator Mass Spectrometry facility. Northern Arizona University followed the H<sub>2</sub>-reactor reduction technique (Vogel et al., 1987) and submitted to the W.M. Keck Carbon Cycle Accelerator Mass Spectrometry Laboratory. Radiocarbon ages were calibrated (cal ka BP) using the IntCal13 curve (Reimer et al., 2013) and used to develop an age-depth model (Blaauw, 2010).

### 2.4. Molecular biomarker extraction and analysis

Lignin was characterized as CuO oxidation products following previous work (Hedges and Ertel, 1982; Louchouart et al., 2010; Shields et al., 2016). A mass of sample containing  $5 \pm 1$  mg OC was loaded into screw-cap, stainless-steel reaction vessels along with  $330 \pm 5$  mg CuO,  $105 \pm 5$  ferrous ammonium sulfate hexahydrate, a stainless-steel ball bearing, and ~2–3 mL N<sub>2</sub>-sparged 2 N sodium hydroxide. Vessels were sealed with Teflon O-rings, loaded onto a rotating carousel within a modified gas chromatograph (GC) oven, heated at 4.2 °C/min to 155 °C, and then held constant for 3 hours. Once cooled, a mixed procedural recovery standard containing 0.5 mg/mL ethyl vanillin and methyl cinnamic acid in methanol was spiked with 50  $\mu\text{L}$  into each vessel. Vessels were centrifuged at 3500 rpm for 5 min and the supernatants were collected in 20-mL screw-cap test tubes. The previous step was repeated twice by adding 1 N sodium hydroxide to each vessel, capping, and loosening the ball bearings by shaking prior to centrifugation. Test tubes were loaded with

2 g sodium chloride, acidified by the addition of 2 mL 6 N HCl, and stored overnight. On the second day, three sequential liquid-liquid extractions were performed by the addition of 3 mL ethyl acetate to each test tube, agitation by vortex mixer, centrifugation (2000 rpm for 2 min), and transfer of the supernatant into glass pipette 'columns' constructed by packing a glass pipette with glass wool and ~1.5 g anhydrous sodium sulfate, which served to simultaneously dry and filter particulates from supernatants. Collected supernatants were concentrated under a gentle stream of N<sub>2</sub>, transferred to 4 mL vials, fully dried by a gentle stream of N<sub>2</sub>, and then stored until analysis. Dried extracts were dissolved in 2 mL anhydrous pyridine and 80  $\mu\text{L}$  was transferred to high-recovery 1.2-mL screw-cap vials. A 2 mg/mL mixture of methyl 3,4-dimethoxybenzoate (ARS) in pyridine was prepared and combined at a ratio of 1:20 with the derivatization reagent N,O-Bis(trimethylsilyl)trifluoroacetamide:trimethylchlorosilane (99:1) and then spiked into each sample vial at a volume of 20  $\mu\text{L}$ . Samples were capped, reacted at 70 °C for 1 hour to produce trimethylsilyl derivatives, and then analyzed on a ThermoFisher Trace 1310 GC coupled to a ThermoFisher TSQ 8000 triple quadrupole mass spectrometer (MS/MS). Samples (1  $\mu\text{L}$ ) were injected into a deactivated, 4 mm diameter recessed gooseneck liner with glass wool insert (SGE Analytical Science, USA) at a split ratio of 20:1 using He as the carrier gas (1 mL/min), with the injector temperature maintained at 260 °C. The GC column (DB-5 ms, 0.25-mm diameter  $\times$  30-m length, 0.25- $\mu\text{m}$  film thickness, Agilent, USA) was held at 85 °C for 1 min after injection, ramped at 4 °C/min until 216 °C, ramped at 10.3 °C/min until 270 °C, and held constant for 6 min. The transfer line between the GC and MS/MS was held at 280 °C and the MS/MS electron ion source was held at 250 °C and an energy of 70 eV. MS/MS transitions were optimized using lignin-phenol standards by manufacturer software, and the top three products from the top precursor ion for each compound were monitored to ensure identification. Peak areas were converted to relative response factors to ARS and calibrated to concentrations using a seven-point, external, log-log transformed, third-order polynomial calibration curve, following previous approaches with modifications for our analytical setting (Hernes and Benner, 2002; Spencer et al., 2010).

Total hydrolyzable amino acids were extracted and quantified following Hutchings et al. (2018). In brief, samples containing  $3 \pm 1$  mg OC were added to 20 mL screw-cap test tubes and 1 mL of 6 N HCl was added to each test tube. The headspace of each test tube was flushed with N<sub>2</sub> and then each tube was capped with PTFE-lined caps and placed in a muffle furnace at 110 °C for 20 h. Following hydrolysis, tubes were allowed to cool and then diluted with 5 mL of H<sub>2</sub>O. Aliquots of 0.15 mL from each tube were further diluted ten-fold using H<sub>2</sub>O and then filtered through 0.2  $\mu\text{m}$  nylon membrane syringe filters into 1.5 mL vials for analysis. Analysis was achieved using a ThermoFisher Ultimate 3000 RS liquid chromatograph coupled to a ThermoFisher TSQ Endura triple quadrupole mass spectrometer (LCMS). Separation was achieved with a Hypersil Gold aQ C18 reversed-phase column (20  $\times$  2.1 mm I.D., 1.9  $\mu\text{m}$

particle size, Unity Lab Services #00109-01-00013) fitted with a pre-column filter (ThermoFisher #88200). Separation was isocratic and used a mobile phase consisting of 10 mM perfluoropentanoic acid in H<sub>2</sub>O with 8% by volume acetonitrile, a total duration of 3.5 min, and a flow rate of 0.5 mL/min. After 3.5 min, flow was changed to 100% methanol at 0.5 mL/min for 2.5 min to flush the column and clean the ion source. Eluent from the Ultimate 3000 was introduced to a heated electrospray ion source operated at 4000 V, with a vaporizer temperature of 200 °C, an ion-transfer tube temperature of 300 °C, and with N<sub>2</sub> drying/nebulizing gas with sheath and auxiliary flows of 32.5 and 10 arbitrary units, respectively. The TSQ Endura was operated in tandem mass spectrometry mode with a cycle time of 1 s, a 1.5 mTorr pressure of argon in the collision cell, and Q1 and Q3 mass resolutions set to 0.7 m/z full width at half maximum. Mass transitions were determined by infusion of individual standards. Quantification was achieved using one-point standard addition, where 1.5 µL of sample was introduced with either 1.5 µL of blank (0.1 N HCl in H<sub>2</sub>O) or 1.5 µL of mixed standard (40 µM of each amino acid in 0.1 N HCl in H<sub>2</sub>O). This approach ensured standards were analyzed in the same sample matrix they calibrated, and the increase in instrument response due to the known standard concentration was used to calculate the unknown sample concentration (Ellison and Thompson, 2008).

Branched glycerol dialkyl glycerol tetraethers (brGDGTs) were extracted and analyzed following (Hopmans et al., 2016). Samples containing 50 ± 5 mg OC were loaded into ~34 mL stainless steel extraction vessels and extracted on a Dionex Accelerated Solvent Extractor 300. The extraction solvent was 9:1 (v:v) methylene chloride:methanol applied at 100 °C in three cycles with a static time of 5 min and a 50% flushing volume. The initial extracts were dried under a gentle stream of N<sub>2</sub>. Glass-wool-plugged glass pipette columns containing ~1 g alumina (activated at 150 °C for 2 h) were used to separate the extracts using the following scheme: dried extracts were dissolved in ~1 mL of a mobile phase, loaded onto the column and allowed to flow under gravity, collected in a labeled vial, and the same mobile phase was repeated twice for a total of three column volumes. Two mobile phases, 9:1 (v:v) hexane:methylene chloride and 1:1 (v:v) methanol:methylene chloride were applied sequentially under this scheme to yield ‘apolar’ and ‘polar’ fractions, respectively. The ‘polar’ fraction was dried under N<sub>2</sub>, dissolved in 99:1 (v:v) hexane:isopropanol, and filtered through a 0.45 µm PTFE syringe filter into a vial for analysis. Analysis was performed on the same LCMS instrument as amino acids. Separation was achieved using the same columns, mobile phases, column temperature, and flow rate as described in Hopmans et al. (2016) but with an injection volume of 10 µL. Ionization was performed using an atmospheric pressure chemical ionization source in positive mode with a discharge current of 5 µA, vaporizer temperature of 350 °C, and nebulizing gas flows of 15, 1, and 4 arbitrary units of N<sub>2</sub> for the sheath, auxiliary, and sweep gases, respectively. The ion transfer tube was operated at 250 °C and the mass spectrometer was operated in full scan mode

with a range of 900–1500 m/z, a rate of 500 Da/sec, and a resolution of 0.7 m/z full width at half maximum. Assignments were based on extracted ion chromatograms of the appropriate primary ions with reference to published chromatograms (De Jonge et al., 2014; Hopmans et al., 2016).

## 2.5. Molecular biomarkers

Eleven lignin-derived phenols (see Fig. A1 for phenol and compound-family abbreviations) were calculated relative to OC (mg/100 mg OC) following convention. Total lignin was defined as VSC, or the sum of V, S, and C phenols. Lignin acid to aldehyde ratios of either the vanillyl (Ad:Al<sub>V</sub>) or syringyl (Ad:Al<sub>S</sub>) were used to estimate the amount of fungal degradation of lignin (Hedges et al., 1988; Opsahl and Benner, 1995). The lignin non-woody to woody tissue index (C:V) was used to estimate plant tissue contributions (Ertel and Hedges, 1984).

Amino acids included a suite of proteinogenic amino acids (ThermoFisher #20088) as well as the secondary amino acids *trans*-4-hydroxy-L-proline (Hyp), 2,6-diaminopimelic acid (DAPA), gamma-aminobutyric acid (GABA), and muramic acid (MurA), which were purchased from Sigma-Aldrich. Individual compound concentrations are calculated relative to OC (µmol/g OC). The proportion of total hydrolysable amino acid-derived N as a percentage of TN (AA-N%) was also calculated by converting the molecular weight of each amino acid to N content relative to TN. AA-N% typically decreases with soil organic matter degradation (Schmidt et al., 2000; Hobara et al., 2014; Philben et al., 2016). An amino acid degradation index was calculated using the first principal component axis of the mole-percent concentrations of all detected amino acids using the following equation:

$$\text{Degradation Index (DI)} = \sum_{i=1}^i \left( \frac{\text{AA}_i - \text{mean}_i}{\text{SD}_i} \right) \times \text{PC}_i \quad (1)$$

where *i* is a vector including all analyzed amino acids, AA<sub>*i*</sub> is the mole-percent abundance of the amino acid within a sample, mean<sub>*i*</sub> is the mean mole percent abundance of the amino acid within the data set, SD<sub>*i*</sub> is the standard deviation of the mole percent abundance of the amino acid within the data set, and PC<sub>*i*</sub> is the first principal component loading of the amino acid from a principal component analysis of all samples (Dauwe et al., 1999). This approach requires a range of sample states from ‘fresh’ to ‘degraded’ and operates under the hypothesis that the amino acid composition of a soil or sediment samples shifts from primary-producer-dominance to microbial-dominance during processing, and has been applied in a variety of aquatic and terrestrial study systems (Dauwe et al., 1999; Duan and Bianchi, 2007; Menzel et al., 2015; Philben et al., 2016). DI ranges from negative to positive values, and directionality with degradation must be inferred from other sample characteristics (e.g., TOC, C: N). We rescaled the DI from Eq. (1) using the following calculation:

$$\text{DI}_{\text{rescaled}} = \text{DI}_{\text{raw}} + |\text{DI}_{\text{min}}| \quad (2)$$

where  $DI_{\text{raw}}$  is the unmodified DI for a given sample and  $DI_{\text{min}}$  is the minimum DI from the data set. For this data set, this results in a DI of zero, corresponding to the ‘fresh-est’ sample and increasing values indicating progressive degradation. All DI values reported here have been rescaled in this way.

Both 5-methyl and the recently demonstrated 6-methyl br-GDGTs were detected, but the latter were much less abundant and only 5-methyl br-GDGTs are reported here (Weijers et al., 2007; De Jonge et al., 2014; Hopmans et al., 2016). The  $MBT'_{5ME}$  index was calculated using the following equation:

$$MBT'_{5ME} = \frac{(Ia + Ib + Ic)}{(Ia + Ib + Ic + IIa + IIb + IIc + IIIa)}$$

where the Roman numerals I, II, and III correspond to tetra-, penta-, and hexa-methylated br-GDGTs, respectively, and the lowercase letters a, b, and c correspond to the presence of zero, one, or two cyclopentane moieties, respectively. The  $MBT'_{5ME}$  index was transferred to temperature using the De Jonge et al. (2014) equation:

$$MAT_{-5ME} = 31.45 \times MBT'_{5ME} - 8.57$$

In addition, the uncalibrated  $MBT'_{5ME}$  index was used as a stratigraphic biomarker.

## 2.6. Statistical approach

Data were analyzed using the R statistical software (R Core Team, 2017). All statistical hypothesis testing was achieved by application of a balanced bootstrap approach, using an appropriate sampling statistic (Davison et al., 1986). The 95% confidence intervals of the statistic (e.g., arithmetic mean, ordinary least squares slope) were used

to test for a significant difference from zero, which is equivalent to a  $p$ -value cutoff of 0.05 for null hypothesis testing.

## 3. RESULTS

### 3.1. Physical description

Described from top to bottom, the surface ~60 cm of the core consists of an organic-rich soil and generally coincides with the contemporary active layer. The uppermost ~15 cm is an organic mat containing both live and dead plant material. This section has abundant pore ice until the appearance of discontinuous, horizontal 3- to 4-mm-thick ice lenses at 50–54 cm, which likely marks the base of the contemporary active layer. This value is within the observed range of active layer depths for this locality (~40 to 130 cm) while mean active layer depths tend to be from ~55 to 75 cm (Hutchings et al., 2017). Mineral content increases towards the bottom of the active layer, however this section is organic-rich throughout.

Relict, frozen soil below the active layer is silty and gray, and dry bulk density increases with depth (Fig. 2). Ice lenses throughout the core range from 1 to 7 mm thick, with the thickest ice lenses observed between 100 and 230 cm. Suspended ice structures in the 99–120 and 134–157 cm depth intervals indicate cryoturbation. Granular and pebble gravel inclusions are first observed at 80 cm and are present throughout the core, most commonly in the 250–305 cm interval.

Brown silt begins at 305 cm and contains sub-angular pebbles with ~1 mm ice lenses until 405 cm. Between 405 and 433 cm, the brown silt grades to a peat that continues until 513 cm. The dark brown peat contains abundant plant macrofossils including a ~4 cm diameter piece of wood. Below 513 cm, the core is a gray silt with frequent pebbles

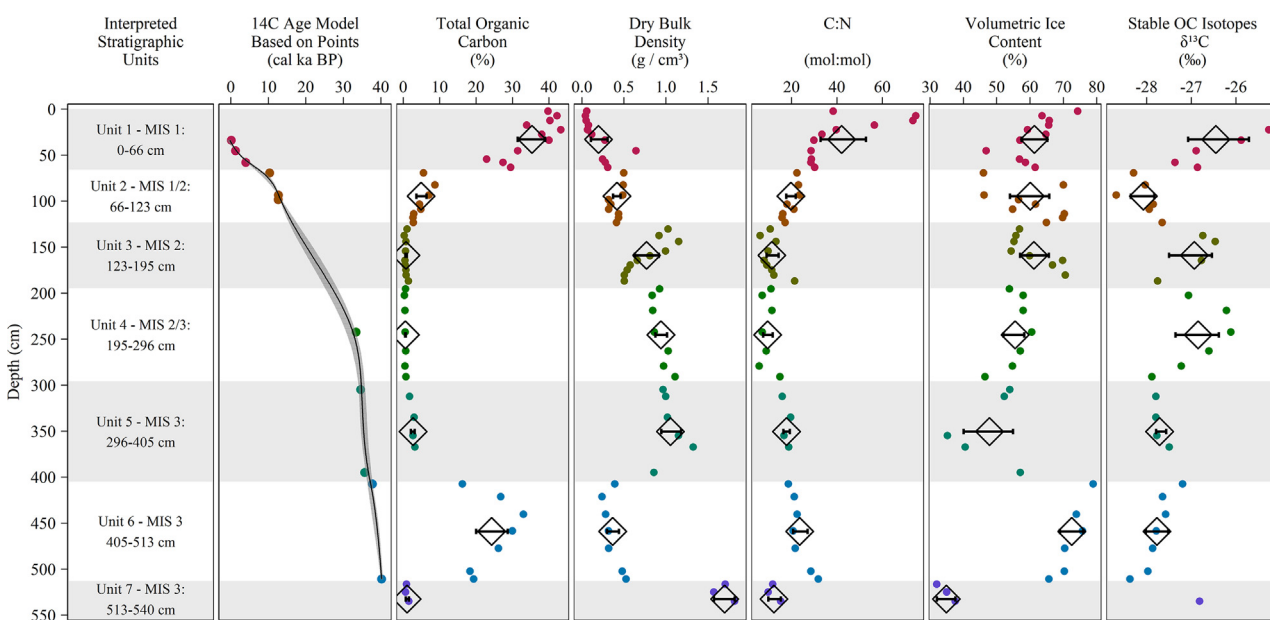


Fig. 2. Downcore bulk geochemical profiles for a 5.4-m-long, upland permafrost core from Eight Mile Lake, Alaska. The age model is based on 11  $^{14}\text{C}$  plant macrofossils and described in detail in the text. Interpreted stratigraphic units are based on bulk and biomarker indices. Black diamonds represent the mean value within a unit and their error bars are the 95% confidence interval.

that extend downward to 540 cm, where further coring was terminated by contact with an obstruction. Based on previous drilling at this site, the core probably did not extend to bedrock (Osterkamp, 2005).

### 3.2. Geochronology

Fourteen macrofossils or macrofossil assemblages were analyzed for radiocarbon initially (Table A1), but three samples were rejected as outliers, with two dates (depths 120–127, 157–162 cm) showing anomalously young ages and one (depth 350–360 cm) showing an anomalously old (radiocarbon-dead) age. The young outliers are within a section of low TOC and likely represent surface material entrained in the core barrel during the coring operation. The coring device used for permafrost retrieval uses relatively blunt steel teeth that grind into the soil and cause some thawing during the process, and due to the frequent retrieval of the core barrel (every ~25–50 cm), the possibility of surficial plant material falling into the borehole cannot always be eliminated. This is typically resolved during processing by discarding the outer ~5–10 mm of the core to avoid contamination. The old outlier contains charcoal and is likely pre-aged, reworked material from upslope. The final age-depth model consists of 11 radiocarbon ages (Fig. 2) and indicates rapid apparent accumulation during MIS 3 (~0.37 mm/yr) and slower apparent accumulation during MIS 1 and 2 (~0.04 mm/yr). MIS 2 sedimentation rate was interpolated because of an absence of dateable macrofossils (Fig. 2). The age-depth model used here assumes absence of erosional unconformities through the undated section that spans from 33.3 to 12.7 cal ka BP.

### 3.3. Bulk biogeochemistry

TOC is highest within the contemporary active layer and the buried peat section (Fig. 2). The lowest TOC is found between 125 and 300 cm, which corresponds to ~15 to ~34 ka. The same trends are generally observed for organic carbon to total nitrogen molar ratios (C:N), where high values correspond to TOC-rich sections and lower values to TOC-poor sections. This core contains 74 kg OC/m<sup>2</sup> to 3 m depth and 208 kg OC/m<sup>3</sup> to 5 m depth. The  $\delta^{13}\text{C}$  varies from -28.7 to -25.3‰ (Fig. 2), with the highest values observed within the active layer and the lowest values immediately below it, which is generally opposite expectations for a soil profile (Natlhofer and Fry, 1988; Boström et al., 2007). There is no apparent trend in  $\delta^{13}\text{C}$  farther downcore, although the deeper, organic-rich section has consistently more depleted values compared to the active layer. No significant relationship is present between C:N and  $\delta^{13}\text{C}$  ( $r^2 = 0.08$ ,  $p > 0.05$ ).

### 3.4. Lignin biomarkers

Total OC-normalized lignin phenols, VSC, is relatively low in the uppermost organic mat (Fig. 3) and increases to a value of 2 mg/100 mg OC at ~30 cm until the bottom of the Holocene section. Total lignin phenols remained <1 mg/100 mg OC throughout the OC-poor section until the transition to brown silt at 305 cm. VSC progressively increases below 305 cm to values between 4 and 5 mg/100 mg OC with the highest values in the buried peat between 405 and 513 cm, which were significantly greater than VSC values throughout the rest of the core

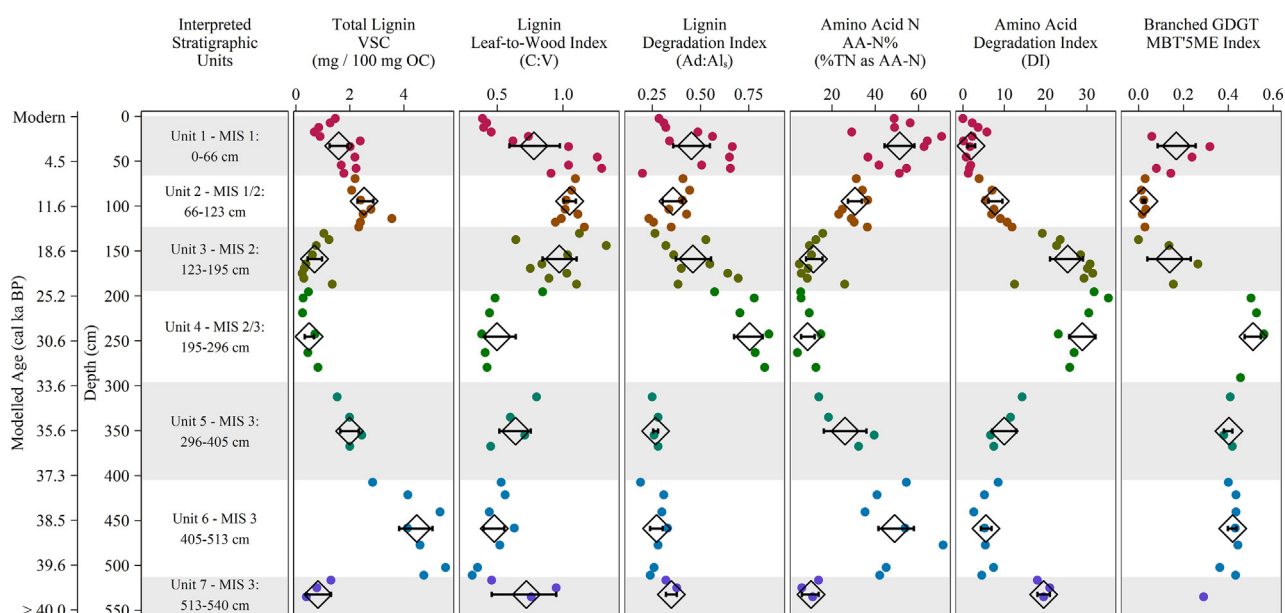


Fig. 3. Bulk molecular geochemical profiles. The age y-axis is based on the age model shown in Figure. Lignin C:V values close to zero indicate woody tissues and increasing values indicate non-woody tissues. Lignin Ad:Al<sub>s</sub> and amino acid degradation index (DI) are both oriented such that well-preserved samples have low values that increase with degradation. Black diamonds represent the mean value within a unit and their error bars are the 95% confidence interval.

( $p < 0.05$ ). VSC in samples below 513 cm return to  $< 1$  mg/100 mg OC.

The lignin leaf-to-wood tissue index, C:V, is low within the uppermost organic mat (Fig. 3) and consistent with more woody tissues in this layer, which is opposite from expectations of non-woody tissue inputs from the dominant sedge, *E. vaginatum* and may be driven by dwarf shrubs that are also present. Coincident with the increase in total lignin at 30 cm, C:V shifts to non-woody values and remains high ( $\sim 1$ ), consistent with non-woody tissue inputs throughout the Holocene and post-glacial Pleistocene. Unlike total lignin, these values remain high until a sharp decrease at 200 cm. Below 200 cm to the base of the core, C:V remains low ( $\sim 0.5$ ) consistent with a more woody lignin composition.

The lignin degradation indices Ad:Al<sub>S</sub> and Ad:Al<sub>V</sub> have a strong, positive correlation (not shown,  $r^2 = 0.86$ ,  $p < 0.05$ ) and, for simplicity, only Ad:Al<sub>S</sub> values are reported. Ad:Al<sub>S</sub>, like VSC and C:V, was low ( $\sim 0.25$ ) within the top 30 cm (Fig. 3), consistent with fresh plant tissues. Ad:Al<sub>S</sub> reaches a Holocene maximum of  $\sim 0.6$  near the base of the active layer, consistent with moderately processed lignin. Below the active layer, Ad:Al<sub>S</sub> returns to low values of  $\sim 0.3$  until 125 cm before then increasing to a maximum  $\sim 0.75$  between 200 to 305 cm, consistent with highly processed lignin. A sharp decrease is observed at the transition to brown silt at 305 cm, and the low, ‘fresh’ Ad:Al<sub>S</sub> values persist for the remainder of the core.

### 3.5. Amino acid biomarkers

Total hydrolyzable amino acid N as a percentage of total soil N, AA-N%, is variable but high within the active layer (Fig. 3), ranging from 29.1 to 70.6%. Below the active layer, AA-N% decreases to a minimum of 5–10% by 150 cm and generally remain well below 20% until 350 cm, which is deeper than the transition from gray to brown silt at 305 cm. Below 350 cm, AA-N% increases and averages 46% until the base of the brown peat at 513 cm. Below 513 cm, AA-N% returns to low values, comparable to those in the 150–350 cm depth interval.

An amino acid degradation index, DI, was calculated based on principal component analysis in Fig. A2. The first two principal components explain 76.6% of the total variance. The first principal component axis, PC1, has the most negative loadings for active layer samples and the most positive loadings for samples between 125 cm and 300 cm. Among the amino acids with positive loadings are the microbial cell-wall biomarkers MurA and DAPA and the secondary amino acid GABA. DI has a negative logarithmic relationship with TOC ( $r^2 = 0.83$ ,  $p < 0.05$ , not shown) and TN ( $r^2 = 0.59$ ,  $p < 0.05$ , not shown). The relationship between DI and C:N is similar to TOC and TN (i.e., non-linear, but negative) and also improves upon log<sub>10</sub>-transformation of C:N ( $r^2 = 0.71$ ,  $p < 0.05$ , not shown). AA-N%, a more ‘bulk’ measure of organic N quality compared to DI due to the loss of molecular information, has a strong, negative relationship with DI ( $r^2 = 0.87$ ,  $p < 0.05$ , Fig. 4a). Downcore (Fig. 3), DI has lowest values within the active layer that grade to highest values found near

200 cm. DI returns to low values within the peat between 405 and 513 cm. The section below 513 cm returns to values similar to those in the middle section of the core, much as was seen for VSC and AA-N%.

The plant cell-wall biomarker Hyp is correlated with VSC throughout the core ( $r^2 = 0.63$ ,  $p < 0.05$ , Fig. 5a), consistent with a shared source from plants. The secondary amino acid GABA, formed through decarboxylation of glutamic acid (Glu), is also positively correlated to DAPA ( $r^2 = 0.75$ ,  $p < 0.05$ , Fig. 5b), consistent with previous findings that GABA accumulates by microbial processing. The GABA to Glu ratio is also correlated to DI ( $r^2 = 0.94$ ,  $p < 0.05$ , Fig. 4b). The two microbial amino acids MurA and DAPA are correlated positively ( $r^2 = 0.49$ ,  $p < 0.05$ , Fig. 5c), although the relationship is weakened upon removal of the sample with an influential MurA concentration of 13.6  $\mu\text{mol/g}$  OC ( $r^2 = 0.29$ ,  $p < 0.05$ , not shown). However, the influential point was analyzed in duplicate and overall procedural precision was 14% for this data set, which indicates that this value is not an analytical artefact.

### 3.6. Branched-glycerol dialkyl glycerol tetraether biomarkers

Branched GDGTs were summarized by their degree of methylation (MBT'<sub>5ME</sub> index, Fig. 3) and then converted to mean annual temperature using existing, global transfer functions (De Jonge et al., 2014). The MBT'<sub>5ME</sub> index in Units 2 and 3 is lower than the minimum values observed in the global dataset (De Jonge et al., 2014). The MBT'<sub>5ME</sub>-based MAT (Fig. A3) within the active layer varies with an average and standard deviation of  $-3.1 \pm 3.9$  °C that decreases to an average and standard deviation of  $-7.4 \pm 1.4$  °C below the active layer until a depth of 140 cm. At 140 cm, reconstructed MAT increases to a maximum between 200 and 240 cm of  $8.1 \pm 0.9$  °C. Below 240 cm, the reconstructed MAT is relatively constant at  $4.6 \pm 0.9$  °C until the base of the buried peat at 513 cm. The positive reconstructed MAT below 140 cm is opposite expectations and indicates this conversion is not appropriate for this core.

The degree of cyclization (CBT<sub>5ME</sub> index) cannot be calculated for samples shallower than 140 cm, as they do not have br-GDGTs Ib or IIb and the CBT<sub>5ME</sub> is the log<sub>10</sub>-transformation of the cyclization ratio (Weijers et al., 2007; De Jonge et al., 2014). The cyclization ratio is zero for those samples, and this feature co-occurs where the microbial amino acid MurA is also not detected (Fig. 5c inset), suggesting a potential shift in microbial community or relative abundance at that depth. While the modern setting is that of a moist, acidic tundra, non-zero concentrations of TIC between 100 and 250 cm depth (Fig. A3) suggests that this state was not constant through time, although the CBT<sub>5ME</sub>-based pH reconstruction (Fig. A3) indicates consistently acidic conditions.

### 3.7. Interpreted stratigraphic units

Stratigraphic unit boundaries within this core were identified by a combination of visual appearance of the sedi-

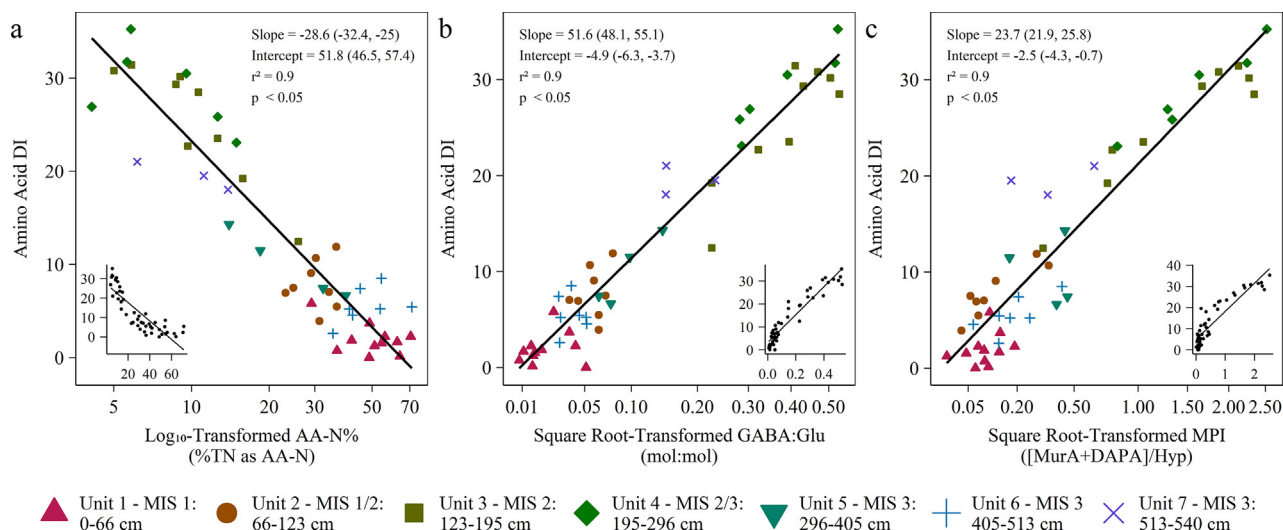


Fig. 4. Scatter plots of the amino acid degradation index against other amino acid indices, including (a) percent TN as amino acid N (AA-N %), (b) gamma-aminobutyric acid: glutamic acid (GABA:Glu), and (c) the microbial-plant index (MPI). Each index has been transformed as necessary to improve linearity, and the original, untransformed relationships are shown as insets. Regression coefficients are of the transformed relationships and the 95% confidence intervals are shown in parentheses.

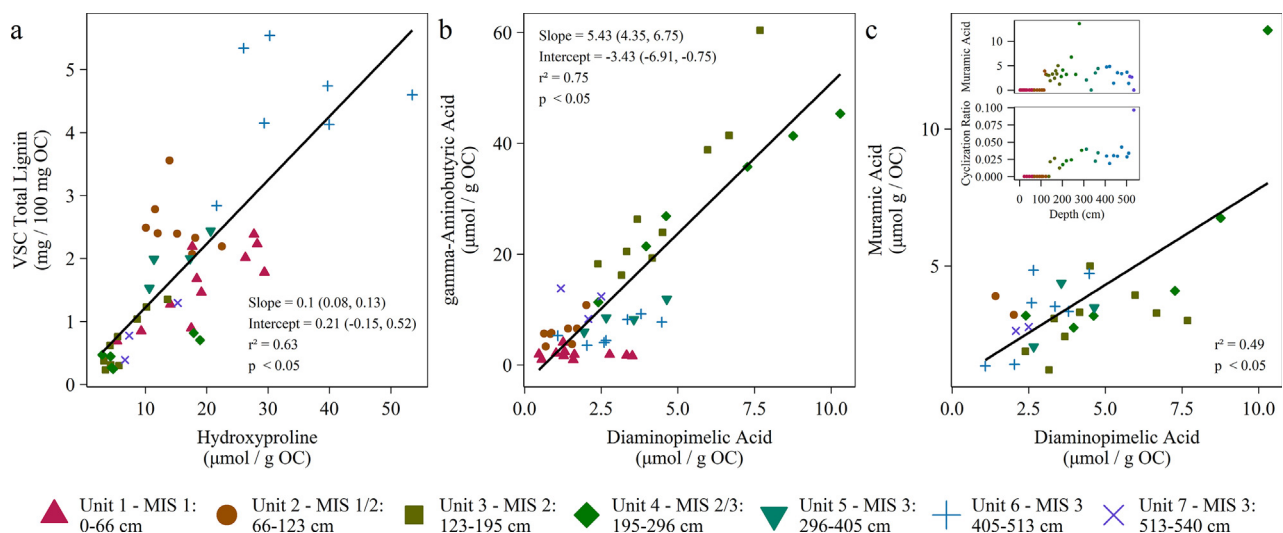


Fig. 5. Scatter plots showing relationships between molecular indices and markers. Hyp is correlated with total lignin (a), the bacterial amino acid DAPA is correlated with GABA (b), and the two bacterial biomarkers DAPA and MurA are correlated (c). The cyclization ratio of the panel c inset is calculated from Weijers et al. (2007). The 95% confidence interval of each regression coefficient is shown in parentheses.

ment and shifts in bulk and biomarker properties (Figs. 2 and 3), as described in the following sections. A principal components analysis (Fig. 6) of the bulk and geochemical indices supports this approach and indicates decreasing OC quality with increasing principal component 1 loadings.

### 3.7.1. Unit 1 – MIS 1: 0–66 cm (0–4.6 ka)

Unit 1 encompasses the modern active layer and includes material that accumulated during the last ~5 ka. The interpreted base of the active layer at 50–54 cm (see Section 3.1) coincides with the shift from organic- to mineral-dominated contents at 60–70 cm. Material within this unit is both vertically accreted (i.e., increase in observed

$^{14}\text{C}$  age with depth) as well as mixed by cryoturbation and plant activity (Hicks Pries et al., 2011). The OC within the unit is the least degraded within this core according to both bulk (C:N) and biomarker (Ad:Al<sub>s</sub>, DI) indices and is distinguished by negative PC1 loadings (Fig. 6).

### 3.7.2. Unit 2 – MIS 1/2: 66–123 cm (4.6–15. ka)

The material that accumulated during the latest, post-glacial Pleistocene and early Holocene shows generally stable values for bulk and biomarker geochemical indices (Figs. 2 and 3, respectively). Lignin C:V indicates consistently non-woody organic matter composition, whereas lignin Ad:Al<sub>s</sub> indicates less lignin degradation compared to

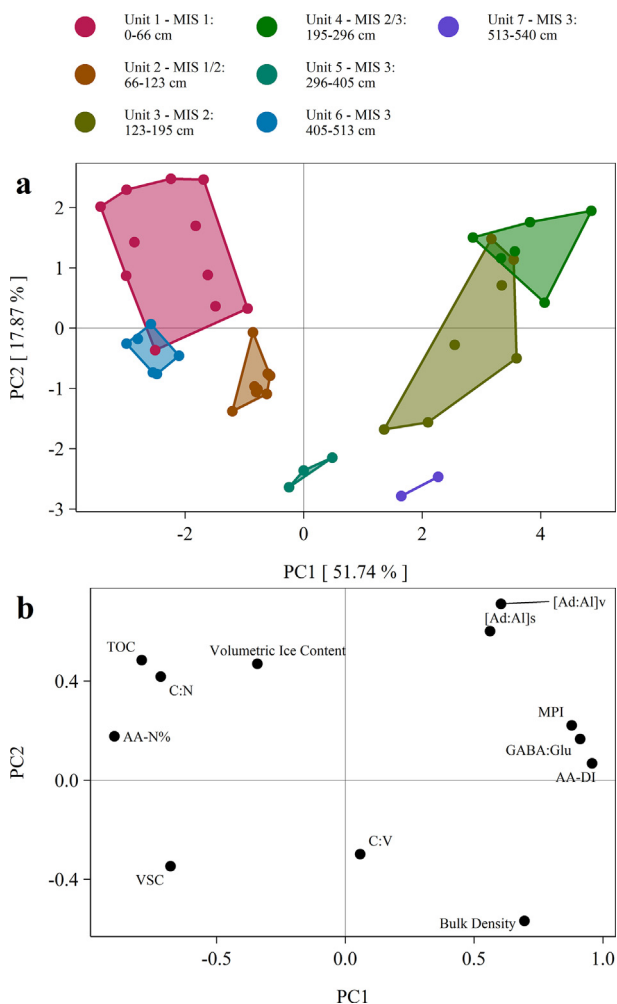


Fig. 6. Bulk and biomarker data principal component analysis showing separation between stadial and interstadial units. Top panel (a) shows sample loadings and bottom panel (b) shows variable loadings. Branched-GDGT data is not used here due to less frequent sampling.

Unit 1. The amino acid DI grades to progressively higher values through this section. AA-N% and DI do not, however, agree with the low, ‘fresh’ lignin Ad:Al<sub>s</sub> values, suggesting the potential for preferential preservation of lignin, perhaps related to the increased mineral content (Hernes et al., 2013).

### 3.7.3. Unit 3 – MIS 2: 123–195 cm (15.2–25.8 ka)

The transition between Units 2 and 3 is marked by an increase in bulk density caused by lower ice content, a 1‰ shift in  $\delta^{13}\text{C}$ , a ~50% decrease in lignin VSC, decreases in AA-N%, and increases in Ad:Al<sub>s</sub> and DI (Figs. 2 and 3). Branched GDGT MBT<sub>5ME</sub> begins to increase and cyclized br-GDGTs appear with this unit (Fig. 5c inset). All samples within this unit plot to more positive PC1 values in Fig. 6.

### 3.7.4. Unit 4 – MIS 2/3: 195–296 cm (25.8–34.5 ka)

Units 3 and 4 are separated by a sharp increase in MBT<sub>5ME</sub> at 200 cm and the most positive PC1 values in

Fig. 6. All metrics on the extent of degradation indicate that the organic matter in this unit is well-processed. The low lignin-phenol C:V indicates predominantly woody plant materials, but TOC and lignin-phenol VSC are so low that alteration of the lignin composition is expected and may be due to preferential preservation of woody lignin (Hedges et al., 1988; Hernes et al., 2007).

### 3.7.5. Unit 5 – MIS 3: 296–405 cm (34.5–36.7 ka)

A reversal in organic matter composition and degradation coincides with the shift to brown silt at the Unit 4/5 transition and to more negative PC1 scores (Fig. 6). Lignin-phenol VSC increases from the minimum observed in Units 3 and 4, indicating increased plant organic matter with corresponding ‘fresh’ Ad:Al<sub>s</sub> values, which are constant throughout this unit. The uppermost sample of Unit 5 has elevated lignin-phenol C:V, which is indicative of non-woody plant cover and consistent with regional paleoecological interpretations of the stadial ‘steppe-tundra’ grassland (Zimov et al., 2009). AA-N% and DI increase and decrease, respectively, indicating a downcore shift to better preservation, potentially a consequence of short active layer residence times (see Section 4.4).

### 3.7.6. Unit 6 – MIS 3: 405–513 cm (36.7–40.1 ka)

The top of Unit 6 marks the first observation of a peat with low ice content that continues to the base of the unit (Fig. 2). Large woody debris and the high lignin-phenol VSC are evidence of the presence of forest vegetation. Lignin Ad:Al<sub>s</sub> and amino acid DI both indicate excellent preservation, comparable to the surface of Unit 1.

### 3.7.7. Unit 7 – MIS 3: 513–540 cm (>40.1 ka)

Unit 7 has bulk and biomarker characteristics similar to Units 3 and 4 (Fig. 7) consistent with a return to cold climate conditions and highly-degraded sediments. This unit has, however, much higher bulk density (Fig. 2) and lacks observable ice lenses. No  $^{14}\text{C}$  dates were analyzed from this unit, so no soil accumulation rate or duration are calculated.

## 4. DISCUSSION

### 4.1. Carbon stocks & accumulation

The Holocene carbon stocks shown here (Fig. 7) are in general agreement with previous work from this site by Hicks Pries et al. (2011) who report stocks of 55–69 kg OC/m<sup>2</sup> in the top meter compared to the 64.6 kg OC/m<sup>2</sup> observed in this core. Observed total accumulation within Unit 1 of this core ( $10.8 \pm 4.1$  g OC/m<sup>2</sup>/yr) is intermediate between the ‘decadal’ and ‘millennial’ average accumulation rates of 25.8 and 2.3 g C/m<sup>2</sup>/yr, respectively, reported by Hicks Pries et al. (2011). The differences are primarily driven by our continuous downcore age-model as well as the deeper layers included in Unit 1, whereas Hicks Pries et al. (2011) consider accumulation only to the base of the active layer. Active layer accumulation rates in either approach are an overestimate compared to units within permafrost because the surficial OC stocks

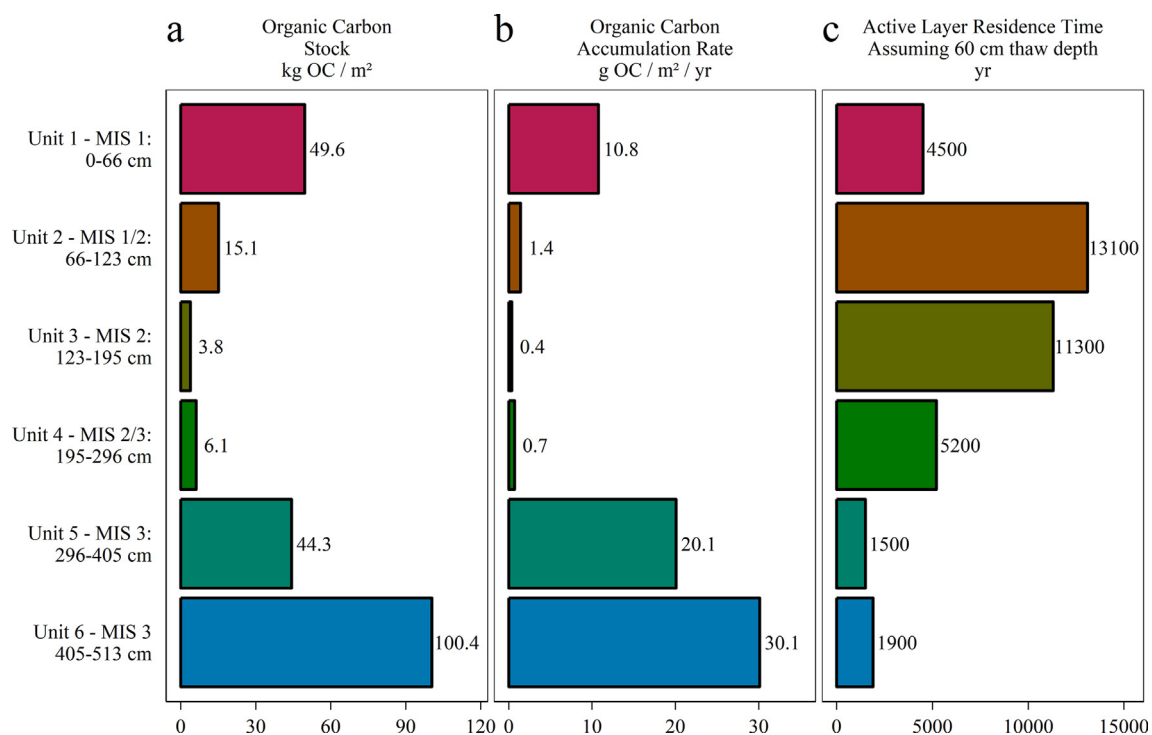


Fig. 7. Bulk organic carbon stock characteristics for each interpreted stratigraphic unit, including depth-integrated OC stocks (a), accumulation rates (b), and the diagnostic active layer residence times (c). Units are described in the text, and Unit 7 is excluded because of its unknown lower extent.

are decomposed within the active layer before sequestration in permafrost, a process which has already occurred for permafrost units.

Organic carbon stocks and accumulation rates were highly variable during the late Pleistocene (Fig. 7). Within the stadial Units 3 and 4, rates were extremely low, consistent with a decrease in productivity and associated ground cover under cold climate conditions due to proximity of this site to the LGM extent in the Alaska range (Fig. 1). A reduction in linear sedimentation rate is seen through many profiles in Siberia and Alaska (Anderson and Lozhkin, 2001; Schirmer et al., 2016; Lapointe et al., 2017). In contrast, stocks and accumulation rates are much higher in the mineral-rich Unit 5 and organic-rich Unit 6 with the observed OC accumulation rates of two to three times higher than in post-glacial Unit 1 and an order-of-magnitude difference than Units 2 through 4.

Using an active layer depth of 60 cm as a reference, a diagnostic active layer residence time for soil in a unit can be calculated based on its linear sedimentation rate and vertical extent (Fig. 7). Active layer residence time is similar in effect to the concept of oxygen exposure time in marine sedimentary geochemistry as it captures the duration of maximum transformation prior to burial (Hedges and Keil, 1995). Active layer depth varies and depends on many factors, including vegetation cover, snow cover, and seasonal air temperatures (Shur et al., 2005; Osterkamp et al., 2009). Active layer depth, however, is unlikely to have varied by more than a factor of 2 or 3, whereas linear sedimentation rate varied by more than an order of magnitude. The

active layer residence times in Fig. 7 can be taken as a heuristic estimate of one driver of long-term organic matter accumulation – rapid burial within the permafrost table. This may, in part, explain why the interstadial Units 5 and 6 have higher stocks and accumulation rates than the interglacial Units 1 and 2.

#### 4.2. Geochronology

The assumed slow accumulation, low OC concentration, and lack of usable  $^{14}\text{C}$  ages during the LGM are common in stratigraphic sections collected in Alaska and Siberia (Anderson and Lozhkin, 2001; Kanevskiy et al., 2011; Wetterich et al., 2014). This effect is likely due to decreased plant cover, which is critical for capture and retention of eolian sediment (Muhs et al., 2003). Intensive efforts on an outcrop yielded datable material from this time period at the Itkillik River exposure in northern Alaska (Kanevskiy et al., 2011; Lapointe et al., 2017), however the approach is impractical when analyzing soil cores. The uppermost section of the age model agrees with previous work on Holocene accumulation at this site (Hicks Pries et al., 2011).

#### 4.3. Soil organic matter degradation

The trend of plant to microbial dominance of organic matter with progressive diagenesis is captured by decreasing molar C:N (Kuhry and Vitt, 1996). This decrease in C:N is observed downcore (Fig. 2) from values >50 in the surficial

organic mat to <10 in the section between 125 and 300 cm. C:N throughout much of the core ranges between 10 and 30, and the sensitivity of the metric to distinguish degradation states within this range is unclear. Several factors, including shifts in plant contributions, denitrification, leaching (Kindler et al., 2011), and the presence of *Sphagnum* spp. mosses whose N is derived from atmospheric deposition (Gerdol et al., 2007), can lead to differences in C:N that are caused by soil organic matter degradation.

The bacterial community was indexed by two bacterial amino acid markers, MurA and DAPA, and changes with depth. Although they are positively correlated when co-present, MurA was not detected in the top 120 cm of the core. In addition, the br-GDGT distribution, as summarized by the cyclization ratio (Fig. 5c inset) or MBT<sub>5ME</sub> index (Fig. 3), indicates large shifts in br-GDGT production between Unit 1 and Unit 4 samples. These shifts do not necessarily indicate shifts in the function (e.g., carbon use efficiency, metabolic pathways) of the overall microbial community, but do indicate a bacterial signature stored in these soils that responded to past climate change.

C-normalized Hyp concentrations have been shown to increase with diagenesis in peatlands and some plant tissues (Philben and Benner, 2013; Philben et al., 2014, 2015). Data here do not support preferential preservation as Hyp yields decrease towards the LGM and only increase farther down-core as TOC increases (Fig. 2, Fig. A3). This lack of a consistent increase in mineral-dominated deposits is also observed in boreal forest soils (Philben et al., 2016). Instead, Hyp appears to act as an overall tracer of plant material present and has good correlation with lignin-phenol yield (Fig. 5a), despite the latter only recording vascular plants. Both lignin and Hyp indicate greater plant material in the ‘woody’ interstadial peat materials compared to the surficial, grass-dominated tundra soils, however this may be biased due to higher concentrations within structural (i.e., woody) tissues. In addition, Hyp has weak, but significant ( $p < 0.05$ ) negative relationships with both Ad:Al<sub>S</sub> ( $r^2 = 0.11$ ) and Ad:Al<sub>V</sub> ( $r^2 = 0.23$ ). If Hyp were selectively preserved during plant decomposition, a positive relationship with lignin degradation would be expected.

AA-N% in non-woody plant tissues is typically relatively high (>50%) and these high values are often also observed within organic soil horizons (Cowie and Hedges, 1992; Friedel and Scheller, 2002; Hobara et al., 2014). AA-N% below 50% is common in mineral soils, although the extraction efficiency of mineral-bound amino acids is reduced, which affect the measured amino acid content of samples (Hedges and Hare, 1987; Christensen and Bech-Andersen, 1989; Friedel and Scheller, 2002; Miltner et al., 2009). Despite this potential bias, AA-N% does decrease with litter decomposition (Hobara et al., 2014), and further losses of organic matter during diagenesis is hypothesized to follow this trend (Friedel and Scheller, 2002). The AA-N% downcore profile here (Fig. 3) supports the preferential loss of amino acids with organic matter degradation, with high AA-N% in the surface organic horizon and the deep organic-rich peat, but low AA-N% in mineral soils. Organic soils, however, had highly variable AA-N% that declined consistently only as mineral content increased, which sug-

gests that AA-N% may be insensitive to initial stages of degradation. A possible cause of this apparent insensitivity is that plant species and tissues have variable AA-N%. The heterogeneity of poorly developed organic soils (i.e., containing plant litter in varying stages of decomposition) could thus result in variable AA-N% that has little to no bearing on the extent of degradation (Cowie and Hedges, 1992; Friedel and Scheller, 2002).

The hydrolyzable amino acid composition of soil organic matter can be expected to shift from plant- to microbe-oriented (i.e., autotrophic to heterotrophic) with progressive decomposition. This shift does not appear to be ubiquitous, however, and may be related to the time scale of interest (Christensen and Bech-Andersen, 1989; Friedel and Scheller, 2002). The ordination-based DI generated here (Fig. 3) indicates low degradation within the buried peat that grades to high values towards and within the LGM before returning to low values within the active layer. The relatively ‘smooth’ DI curve throughout the core also supports the continuous, uninterrupted age model used here, as any unconformity-contemporaneous active layer material would be expected to have much higher DI than underlying material (i.e., within the unconformity-contemporaneous permafrost table).

The positive PCA loadings of MurA and DAPA and negative loading of Hyp on the DI (Fig. A2) indicate the potential for these biomarkers to effectively capture the relative plant versus microbial dominance with soil development. A Microbial:Plant Index (MPI) was calculated using the following equation:

$$\text{MPI} = (\text{MurA} + \text{DAPA})/\text{Hyp} \quad (3)$$

using molar concentrations. This index is similar to previous approaches at utilizing source-specific amino acid biomarkers, but for simplicity we made no attempt to apply weights to this index (Philben and Benner, 2013; Philben et al., 2016). MPI has an expected positive relationship with DI (Fig. 4c) given the PCA loadings of the amino acids (Fig. A2). MPI may, however, have an advantage over DI in that it is grounded in obvious biochemical source-specificity and thus may be applicable to a wider array of systems.

The low amino acid DI values within both the active layer and the buried peat suggests that increases in plant productivity are likely to dominate the DI signal (i.e., shift the soil OC to low values) even under warmer climates that induces higher rates of soil OC turnover and, thus, degradation. This may also explain in part, discrepancies between amino acid and lignin degradation indices. The relatively rapid accumulation of the buried peat shows consistently low lignin degradation values, whereas the slowly accumulating active layer shows highly variable lignin degradation values. The relatively extended residence times of plant litter in the modern active layer (discussed further in 4.5) allow for progressive lignin degradation. While amino acid degradation is also ongoing, the overall hydrolyzable amino acid pool may still be plant-dominated due to efficient recycling of amino-acid-derived N within this N-limited system (Schimel and Chapin, 1996; Salmon et al., 2018). The relationship between plants and amino-acid-derived N may

also be a global phenomenon that enables surface soils to have generally plant-oriented amino acid composition even under high rates of turnover (Farrell et al., 2013).

Potentially complementary to either DI or MPI is the ratio of GABA to Glu, which, similar to MPI, is grounded in biochemistry rather than ordination (Cowie and Hedges, 1992; Dauwe et al., 1999; Duan and Bianchi, 2007). The strong correlation with either GABA:Glu or MPI to DI supports the interpretation that PCI indicates the extent of diagenesis. A decarboxylation reaction similar to GABA:Glu is the generation of beta-alanine from aspartic acid (Asp), however beta-alanine was not measured here. There is, however, a weak positive relationship between the mole-percent abundance of Glu to Asp ( $r^2 = 0.16$ ,  $p < 0.05$ ).

The extent of degradation in this core is well-characterized in the overall amino acid composition (DI), as well as source-specific amino acid indices (MPI, GABA:Glu). Lignin acid-to-aldehyde ratios record alteration of lignin composition, but their relationship to the extent of total soil organic matter degradation is questionable. This problem is most obvious within Units 1 and 3 where Ad:Al<sub>S</sub> would suggest comparable lignin quality, whereas bulk metrics and DI show clear differences between these units. This supports a strategy of measuring the extent of degradation through the relative dominance of plant versus microbial organic matter. Given this, it is not surprising that metrics which only assess plant-derived organic matter composition (e.g., lignin phenols, Hyp) appear to poorly measure the ‘total’ extent of degradation. Without explicit assessment (i.e., field or laboratory experimentation), however, the relationship between these indices and true turnover time is still open to question.

Our findings of highly variable OC quality are in agreement with some previous biomarker work on permafrost deposits (Strauss et al., 2015; Jongejans et al., 2018). However, permafrost deposits often lack the typically expected increase in degradation state with age (Stapel et al., 2016; Stapel et al., 2018), and rather are dependent on the paleoenvironment at the time of deposition. When considering the relative size of the OC stocks within the units described here, we find that the majority of permafrost OC is well-preserved, but that the well-preserved OC is present at multiple depths in our core.

#### 4.4. Branched glycerol dialkyl glycerol tetraethers

Reconstructed mean annual temperatures (MAT) from MBT<sub>5ME</sub> (Fig. 3) using the transfer function of De Jonge et al. (2014) appear to provide reasonable MAT estimates only in post-glacial permafrost. The implied mean annual temperatures consistently higher than 0 °C for core depths below 200 cm are untenable for a syngenetic permafrost assemblage and are also contradicted by regional paleoclimate reconstructions (Frenzel, 1992; Wooller et al., 2011; Vandenberghe et al., 2014). However, uncharacterized changes in the seasonality of br-GDGT production may be responsible for the inferred warmer temperatures in the bottom half of the core (Shanahan et al., 2013; Deng et al., 2016). Such a warm season bias would be able to

provide a rationale for above-freezing temperature reconstructions below 200 cm. The directionality of the calibrated temperatures below 200 cm (Fig. A3) indicates no obvious directionality in Units 5 and 6 and somewhat warmer values in Unit 4. If a warm season bias is in effect, then a possible interpretation is that as the warm season grew shorter from MIS3 towards the LGM, production was increasingly focused in the warmer months. The amino acid and lignin biomarker evidence suggests profound changes in productivity during Units 4, 5, and 6 that may be consistent with this interpretation. When using a peat-specific transfer function (Fig. A3, Naafs et al., 2017), the temperatures within the Unit 6 peat are just below 0 °C and may represent a plausible calibration. The timescales and profound changes in OC composition observed here suggests that selection of a single temperature transfer function is unlikely appropriate for the entirety of this core. Although br-GDGTs are produced in lacustrine as well as soil settings, the preservation of syngenetic cryostructures throughout the core excludes the possibility of a lake being present at the coring location during the period of record. However, we cannot rule out the potential for lateral transport of organic matter, especially within the particularly well-processed Units 3 and 4, which may also confound the br-GDGT temperature trends. The distribution of br-GDGTs by degree of methylation (Fig. A4) is broadly compatible with a global br-GDGT compilation (Russell et al., 2018), although Unit 2 and some of Unit 3 fall outside previously observed values due to their extreme predominance of hexamethyl br-GDGTs.

#### 4.5. Paleoenvironmental Insights

The stratigraphic units identified here document major shifts in paleoenvironment of the Eight Mile Lake locality during the last 40 ka. The proximity of the site to MIS 2 glaciers (Fig. 1) and the very low organic carbon suggests decreased plant productivity consistent with the steppe tundra ecotone (Schirrmeister et al., 2013). The lower productivity could explain the low OC stocks, but the OC is also highly degraded, suggesting that the relatively cold temperatures alone are insufficient to explain the state of the glacial-age sediments. Dry conditions leading to well-aerated soils may explain their highly degraded state. The slow sediment accumulation and resulting increase in active layer residence time (Fig. 7) should also contribute to highly degraded organic matter. However, sediment accumulation is also low within Units 1 and 2 where the sum effects of microbial processing are highly variable, reaffirming that primary productivity is responsible for the material available for storage in permafrost and that dry versus wet conditions can influence remineralization rates.

The shortest active layer residence times are estimated for Units 5 and 6 and correspond to the largest stocks and best preservation of organic matter observed within the permafrost units in this core. Under the current mode of permafrost thaw, Units 5 and 6 are currently ‘protected’ by overlying mineral soils. Soils throughout this profile, however, tend to be ice-rich (Fig. 2) and gradual thaw has been observed to lead to development of relatively

deeply thawed (i.e., 1–1.3 m) water tracks that caused surface subsidence (Vogel et al., 2009; Hutchings et al., 2017). Advanced, landscape-level thermokarst and erosional processes (e.g., active layer detachments, retrogressive thaw slumps, thaw lakes) have not been observed directly at the Eight Mile Lake site, but the high ice content of soils does indicate vulnerability to this phenomenon and the region does exhibit these features (Osterkamp, 2005; Hicks Pries et al., 2013).

## 5. CONCLUSIONS

The amount and quality of organic carbon stored within permafrost soils has implications for the magnitude of permafrost carbon feedback to climate warming and resulting permafrost thaw. The 40-kyr record shown here indicates that buried carbon stocks below the permafrost table store substantial quantities of organic carbon in excess of active layer stocks. The existence of buried stocks in unglaciated localities is well known, but their overall spatial extent, and thus, size remains poorly constrained (Strauss et al., 2013). If the MIS 3, mid-Wisconsin interstadial stocks reported here and elsewhere are a common feature of deep permafrost, then the overall size of the deep permafrost carbon pool may be underestimated.

The quality of permafrost carbon measured here varied greatly. Organic matter in MIS 3 units appeared nearly as well preserved as in the modern active layer, whereas units that formed during the LGM were highly degraded. This variability in carbon stocks with respect to diagenetic history is unsurprising, but the variable quantity and quality of permafrost carbon must be considered when considering post-thaw turnover. When considering the relative size of OC stocks and their quality, most of the permafrost OC found in this core is located within Units 5 and 6, is well preserved, and would likely be highly susceptible to remineralization if thawed.

The amino-acid-based assessment related the apparent quality of organic matter to the shift in source from plant to microbial, using both ordination and source-specific indices. This approach is well suited for permafrost soils, whereas the lignin signature was highly variable and possibly more reflective of lignin degradation state and less of overall soil carbon quality. The br-GDGT data were utilized as stratigraphic and bacterial community indicators, but potential issues such as a changing warm season bias or producer community, which are likely effects that drive variability in temperature calibrations of these biomarkers, confounded their use as even relative temperature proxies (De Jonge et al., 2014; Naafs et al., 2017).

The biomarker data shown here indicates this locality is sensitive to environmental changes associated with a changing climate, particularly with respect to carbon storage under varying regimes of sediment accumulation. Although the peat deposit identified here was from a single core, the common occurrence of MIS 3, mid-Wisconsin peat deposits throughout Siberia and Alaska suggests that the conditions that supported Unit 6 of this core is not a local phenomenon. If the Unit 6 peat is a landscape feature, then the Eight Mile Lake area supported an extensive boreal

forest and suggests the ecosystem is susceptible to major vegetation change if the locality becomes warmer and wetter. Transitions between tundra and forest are generally abrupt, and if that occurs, it will result in different fire regimes, ground cover, and thaw depths that would, in turn, influence the fate of deeper permafrost soils (Chapin et al., 2010; Scheffer et al., 2012).

## ACKNOWLEDGMENTS

Funding for this project was supported by the Jon and Beverly L Thompson Endowed Chair of Geological Sciences. This work was based in part on support provided by the following programs: U.S. Department of Energy, Office of Biological and Environmental Research, Terrestrial Ecosystem Science (TES) Program [Award #DE-SC0006982 and updated with DE-SC0014085 (2015–2018)]; National Parks Inventory and Monitoring Program; National Science Foundation Bonanza Creek LTER program [Award #1026415].

Field work was assisted by Xiaowen Zhang and Justin Ledman. Interpretation of biomarker data was assisted through many discussions with M.R. Shields, K. Whitacre, R.S. Anderson, and C. Ebert picked, identified, and processed macrofossils for  $^{14}\text{C}$  analysis, respectively. The manuscript was improved by the detailed feedback of three anonymous reviewers.

## APPENDIX A. SUPPLEMENTARY MATERIAL

Supplementary data to this article can be found online at <https://doi.org/10.1016/j.gca.2019.03.028>.

## REFERENCES

- Anderson P. and Lozhkin A. (2001) Stage 3 interstadial complex (Karginiskii/middle Wisconsinan interval) of Beringia: variations in paleoenvironments and implications for paleoclimatic interpretations. *Quat. Sci. Rev.* **20**, 93–125.
- Arnold S. L. and Schepers J. S. (2004) A simple roller-mill grinding procedure for plant and soil samples. *Commun. Soil Sci. Plant Anal.* **35**, 537–545.
- Blaauw M. (2010) Methods and code for “classical” age-modelling of radiocarbon sequences. *Quat. Geochronol.* **5**, 512–518.
- Blinnikov M. S., Gaglioti B. V., Walker D. A., Wooller M. J. and Zazula G. D. (2011) Pleistocene graminoid-dominated ecosystems in the Arctic. *Quat. Sci. Rev.* **30**, 2906–2929.
- Boström B., Comstedt D. and Ekblad A. (2007) Isotope fractionation and  $^{13}\text{C}$  enrichment in soil profiles during the decomposition of soil organic matter. *Oecologia* **153**, 89–98.
- Brown J., Ferrians Jr. O.J., Heginbottom J. A. and Melnikov E.S. (1997) Circum-Arctic map of permafrost and ground ice conditions. USGS Numbered Ser., 1.
- Chapin F. S., McGuire A. D., Ruess R. W., Hollingsworth T. N., Mack M. C., Johnstone J. F., Kasischke E. S., Euskirchen E. S., Jones J. B., Jorgenson M. T., Kielland K., Kofinas G. P., Turetsky M. R., Yarie J., Lloyd A. H. and Taylor D. L. (2010) Resilience of Alaska’s boreal forest to climatic change. *Can. J. For. Res.* **40**, 1360–1370.
- Christensen B. T. and Bech-Andersen S. (1989) Influence of straw disposal on distribution of amino acids in soil particle size fractions. *Soil Biol. Biochem.* **21**, 35–40.

- Cowie G. L. and Hedges J. I. (1992) Sources and reactivities of amino acids in a coastal marine environment. *Limnol. Oceanogr.* **37**, 703–724.
- Dauwe B., Middelburg J. J., Herman P. M. J. and Carlo H. R. H. (1999) Linking diagenetic alteration of amino acids and bulk organic matter reactivity. *Limnol. Oceanogr.* **44**, 1809–1814.
- Davison A. C., Hinkley D. V. and Schechtman E. (1986) Efficient bootstrap simulation. *Biometrika* **73**, 555–566.
- Deng L., Jia G., Jin C. and Li S. (2016) Warm season bias of branched GDGT temperature estimates causes underestimation of altitudinal lapse rate. *Org. Geochem.* **96**, 11–17.
- Dlugokencky E. and Tans P. (2017) Trends in atmospheric carbon dioxide. *Earth Syst. Res. Lab. – Glob. Monit. Div.*
- Duan S. and Bianchi T. S. (2007) Particulate and dissolved amino acids in the lower Mississippi and Pearl Rivers (USA). *Mar. Chem.* **107**, 214–229.
- Ellison S. L. R. and Thompson M. (2008) Standard additions: myth and reality. *Analyst* **133**, 992–997.
- Ertel J. and Hedges J. (1984) The lignin component of humic substances: distribution among soil and sedimentary humic, fulvic, and base-insoluble fractions. *Geochim. Cosmochim. Acta* **48**, 2065–2074.
- Farrell M., Hill P. W., Farrar J., DeLuca T. H., Roberts P., Kielland K., Dahlgren R., Murphy D. V., Hobbs P. J., Bardgett R. D. and Jones D. L. (2013) Oligopeptides represent a preferred source of organic N uptake: a global phenomenon? *Ecosystems* **16**, 133–145.
- Faucherre S., Jørgensen C. J., Blok D., Weiss N., Siewert M. B., Bang-Andreasen T., Hugelius G., Kuhry P. and Elberling B. (2018) Short and long-term controls on active layer and permafrost carbon turnover across the Arctic. *J. Geophys. Res. Biogeosci.* <https://doi.org/10.1002/2017JG004069>.
- French H. and Shur Y. (2010) The principles of cryostratigraphy. *Earth-Sci. Rev.* **101**, 190–206.
- Frenzel B. (1992) Atlas of paleoclimates and paleoenvironments of the northern hemisphere eds. B. Frenzel, M. Pecs, and A. A. Velichko. 113.
- Friedel J. K. and Scheller E. (2002) Composition of hydrolysable amino acids in soil organic matter and soil microbial biomass. *Soil Biol. Biochem.* **34**, 315–325.
- Gerdol R., Petraglia A., Bragazza L., Iacumin P. and Brancaleoni L. (2007) Nitrogen deposition interacts with climate in affecting production and decomposition rates in Sphagnum mosses. *Glob. Chang. Biol.* **13**, 1810–1821.
- Goñi M. A. and Hedges J. I. (1995) Sources and reactivities of marine-derived organic matter in coastal sediments as determined by alkaline CuO oxidation. *Geochim. Cosmochim. Acta* **59**, 2965–2981.
- Harden J. W., Koven C. D., Ping C.-L., Hugelius G., David McGuire A., Camill P., Jorgenson T., Kuhry P., Michaelson G. J., O'Donnell J. a., Schuur E. A. G., Tarnocai C., Johnson K. and Grosse G. (2012) Field information links permafrost carbon to physical vulnerabilities of thawing. *Geophys. Res. Lett.* **39**(L15704), 1–6.
- Hedges J. I., Blanchette R., Weliky K. and Devol A. (1988) Effects of fungal degradation on the CuO oxidation products of lignin: a controlled laboratory study. *Geochim. Cosmochim. Acta* **52**, 2717–2726.
- Hedges J. I. and Ertel J. R. (1982) Characterization of lignin by gas capillary chromatography of cupric oxide oxidation products. *Anal. Chem.* **54**, 174–178.
- Hedges J. I. and Hare P. E. (1987) Amino acid adsorption by clay minerals in distilled water. *Geochim. Cosmochim. Acta* **51**, 255–259.
- Hedges J. I. and Keil R. G. (1995) Sedimentary organic matter preservation: an assessment and speculative synthesis. *Mar. Chem.* **49**, 81–115.
- Hernes P. J. and Benner R. (2002) Transport and diagenesis of dissolved and particulate terrigenous organic matter in the North Pacific Ocean. *Deep. Res. Part I Oceanogr. Res. Pap.* **49**, 2119–2132.
- Hernes P. J., Kaiser K., Dyda R. Y. and Cerli C. (2013) Molecular trickery in soil organic matter: hidden lignin. *Environ. Sci. Technol.* **47**, 9077–9085.
- Hernes P. J., Robinson A. C. and Aufdenkampe A. K. (2007) Fractionation of lignin during leaching and sorption and implications for organic matter “freshness”. *Geophys. Res. Lett.* **34**(L17401), 1–6.
- Hicks Pries C. E., Schuur E. A. G. and Crummer K. G. (2011) Holocene carbon stocks and carbon accumulation rates altered in soils undergoing permafrost thaw. *Ecosystems* **15**, 162–173.
- Hicks Pries C. E., Schuur E. A. G., Vogel J. G., Natali S. M., Pries C. E. H., Schuur E. A. G., Vogel J. G. and Natali S. M. (2013) Moisture drives surface decomposition in thawing tundra. *J. Geophys. Res. Biogeosci.* **118**, 1133–1143.
- Hobara S., Osono T., Hirose D., Noro K., Hirota M. and Benner R. (2014) The roles of microorganisms in litter decomposition and soil formation. *Biogeochemistry* **118**, 471–486.
- Hopkins, D. W., Matthews, J. V. and Schweger, C. E. (eds.) (1982) *Paleoecology of Beringia*, first ed. Elsevier.
- Hopmans E. C., Schouten S., Sinninghe and Damsté J. S. (2016) The effect of improved chromatography on GDGT-based palaeoproxies. *Org. Geochem.* **93**, 1–6.
- Hugelius G., Strauss J., Zubrzycki S., Harden J. W., Schuur E. a. G., Ping C.-L., Schirmermeister L., Grosse G., Michaelson G. J., Koven C. D., O'Donnell J. A., Elberling B., Mishra U., Camill P., Yu Z., Palmtag J. and Kuhry P. (2014) Estimated stocks of circumpolar permafrost carbon with quantified uncertainty ranges and identified data gaps. *Biogeosciences* **11**, 6573–6593.
- Hutchings J. A., Bracho R. G. and Schuur E. A. (2017) *Eight Mile Lake Research Watershed, Thaw Gradient: Seasonal Thaw Depth 2004–2016*. BNZ: 519.
- Hutchings J. A., Shields M. R., Bianchi T. S. and Schuur E. A. G. (2018) A rapid and precise method for the analysis of underivatized amino acids in complex natural matrices using volatile-ion-pairing reverse-phase liquid chromatography-electrospray ionization tandem mass spectrometry. *Org. Geochem.* **115**, 46–56.
- Jex C. N., Pate G. H., Blyth A. J., Spencer R. G. M., Hernes P. J., Khan S. J. and Baker A. (2014) Lignin biogeochemistry: from modern processes to Quaternary archives. *Quat. Sci. Rev.* **87**, 46–59.
- De Jonge C., Hopmans E. C., Zell C. I., Kim J.-H., Schouten S., Sinninghe and Damsté J. S. (2014) Occurrence and abundance of 6-methyl branched glycerol dialkyl glycerol tetraethers in soils: implications for palaeoclimate reconstruction. *Geochim. Cosmochim. Acta* **141**, 97–112.
- Jongejans L. L., Strauss J., Lenz J., Peterse F., Mangelsdorf K., Fuchs M. and Grosse G. (2018) Organic matter characteristics in yedoma and thermokarst deposits on Baldwin Peninsula, west Alaska. *Biogeosciences* **15**, 6033–6048.
- Kaufman D. S. and Manley W. F. (2004) Pleistocene Maximum and Late Wisconsinan glacier extents across Alaska, U.S.A. In *Developments in Quaternary Science* pp. 9–27.
- Kanevskiy M., Shur Y., Fortier D., Jorgenson M. T. and Stephani E. (2011) Cryostratigraphy of late Pleistocene syngenetic permafrost (yedoma) in northern Alaska, Itkillik River exposure. *Quat. Res.* **75**, 584–596.

- Kielland K. (1994) Amino acid absorption by arctic plants: implications for plant nutrition and nitrogen cycling. *Ecology* **75**, 2373–2383.
- Kindler R., Siemens J., Kaiser K., Walmsley D. C., Bernhofer C., Buchmann N., Cellier P., Eugster W., Gleixner G., Grunwald T., Heim A., Ibrom A., Jones S. K., Jones M., Klumpp K., Kutsch W., Larsen K. S., Lehuger S., Loubet B., McKenzie R., Moors E., Osborne B., Pilegaard K., Rebmann C., Saunders M., Schmidt M. W. I., Schrupf M., Seyferth J., Skiba U., Soussana J. F., Sutton M. A., Tefs C., Vowinkel B., Zeeman M. J. and Kaupenjohann M. (2011) Dissolved carbon leaching from soil is a crucial component of the net ecosystem carbon balance. *Glob. Chang. Biol.* **17**, 1167–1185.
- Kuhry P., Grosse G., Harden J. W., Hugelius G., Koven C. D., Ping C. L., Schirmer L. and Tarnocai C. (2013) Characterisation of the permafrost carbon pool. *Permafr. Periglac. Process.* **24**, 146–155.
- Kuhry P. and Vitt D. (1996) Fossil carbon/nitrogen ratios as a measure of peat decomposition. *Ecology* **77**, 271–275.
- Lachniet M. S., Lawson D. E. and Sloat A. R. (2012) Revised 14C dating of ice wedge growth in Interior Alaska (USA) to MIS 2 reveals cold paleoclimate and carbon recycling in ancient permafrost terrain. *Quat. Res. (United States)* **78**, 217–225.
- Lapointe L., Talbot J., Fortier D., Fréchet B., Strauss J., Kanevskiy M. and Shur Y. (2017) Middle to late Wisconsinan climate and ecological changes in northern Alaska: evidences from the Itkillik River Yedoma. *Palaeogeogr. Palaeoclimatol. Palaeoecol.* **485**, 906–916.
- Lawrence D. M. and Slater A. G. (2005) A projection of severe near-surface permafrost degradation during the 21st century. *Geophys. Res. Lett.* **32**, 1–5.
- Lindgren A., Hugelius G., Kuhry P., Christensen T. R. and Vandenbergh J. (2016) GIS-based maps and area estimates of northern hemisphere permafrost extent during the Last Glacial Maximum. *Permafr. Periglac. Process.* **27**, 6–16.
- Louchouart P., Amon R. M. W., Duan S., Pondell C., Seward S. M. and White N. (2010) Analysis of lignin-derived phenols in standard reference materials and ocean dissolved organic matter by gas chromatography/tandem mass spectrometry. *Mar. Chem.* **118**, 85–97.
- Mauritz M., Bracho R., Celis G., Hutchings J., Natali S. M., Pegoraro E., Salmon V. G., Schädel C., Webb E. E. and Schuur E. A. G. (2017) Nonlinear CO<sub>2</sub> flux response to 7 years of experimentally induced permafrost thaw. *Glob. Chang. Biol.* **23**, 3646–3666.
- Menzel P., Anupama K., Basavaiah N., Krishna Das B., Gaye B., Herrmann N. and Prasad S. (2015) The use of amino acid analyses in (palaeo-) limnological investigations: a comparative study of four Indian lakes in different climate regimes. *Geochim. Cosmochim. Acta* **160**, 25–37.
- Miltner A., Kindler R., Knicker H., Richnow H. H. and Kästner M. (2009) Fate of microbial biomass-derived amino acids in soil and their contribution to soil organic matter. *Org. Geochem.* **40**, 978–985.
- Muhs D. R., Ager T. A., Bettis E. A., McGeehin J., Been J. M., Begét J. E., Pavich M. J., Stafford T. W. and Stevens D. A. S. P. (2003) Stratigraphy and palaeoclimatic significance of Late Quaternary loess-palaeosol sequences of the Last Interglacial-Glacial cycle in central Alaska. *Quat. Sci. Rev.* **22**, 1947–1986.
- Murton J. and French H. (1993) Thermokarst involutions, summer island, pleistocene mackenzie delta, Western Canadian arctic. *Permafr. Periglac. Process.* **4**, 217–229.
- Naafs B. D. A., Inglis G. N., Zheng Y., Amesbury M. J., Biester H., Bindler R., Blewett J., Burrows M. A., del Castillo Torres D., Chambers F. M., Cohen A. D., Evershed R. P., Feakins S. J., Gałka M., Gallego-Sala A., Gandois L., Gray D. M., Hatcher A., Honorio, Coronado E. N., Hughes P. D. M., Huguet A., Könönen M., Laggoun-Défarge F., Lähenteenoja O., Lamentowicz M., Marchant R., McClymont E., Pontevedra-Pombal X., Ponton C., Pourmand A., Rizzuti A. M., Rochefort L., Schellekens J., De Vleeschouwer F. and Pancost R. D. (2017) Introducing global peat-specific temperature and pH calibrations based on brGDGT bacterial lipids. *Geochim. Cosmochim. Acta* **208**, 285–301.
- Nateller K. J. and Fry B. (1988) Controls on natural nitrogen-15 and carbon-13 abundances in forest soil organic matter. *Soil Sci. Soc. Am. J.* **52**, 1633.
- Opsahl S. and Benner R. (1995) Early diagenesis of vascular plant tissues: lignin and cutin decomposition and biogeochemical implications. *Geochim. Cosmochim. Acta* **59**, 4889–4904.
- Osterkamp T. E. (2005) The recent warming of permafrost in Alaska. *Glob. Planet. Change* **49**, 187–202.
- Osterkamp T. E., Jorgenson M. T., Schuur E. a. G., Shur Y. L., Kanevskiy M. Z. and Vogel J. G. (2009) Physical and ecological changes associated with warming permafrost and thermokarst in Interior Alaska. *Permafr. Periglac. Process.* **256**, 235–256.
- Osterkamp T. E. and Romanovsky V. E. (1999) Evidence for warming and thawing of discontinuous permafrost in Alaska. *Permafr. Periglac. Process.* **10**, 17–37.
- Philben M. and Benner R. (2013) Reactivity of hydroxyproline-rich glycoproteins and their potential as biochemical tracers of plant-derived nitrogen. *Org. Geochem.* **57**, 11–22.
- Philben M., Holmquist J., MacDonald G., Duan D., Kaiser K. and Benner R. (2015) Temperature, oxygen, and vegetation controls on decomposition in a James Bay peatland. *Glob. Biogeochem.* **962–973**.
- Philben M., Kaiser K. and Benner R. (2014) Does oxygen exposure time control the extent of organic matter decomposition in peatlands? *J. Geophys. Res. Biogeosciences* **119**, 897–909.
- Philben M., Ziegler S. E. S., Edwards K. K. A., Kahler R. and Benner R. (2016) Soil organic nitrogen cycling increases with temperature and precipitation along a boreal forest latitudinal transect. *Biogeochemistry* **127**, 397–410.
- R Core Team (2017) *R: A Language and Environment for Statistical Computing*.
- Reimer P. J., Edouard Bard B., Alex Bayliss B., Warren Beck B. J., Paul Blackwell B. G. and Christopher Bronk Ramsey B. (2013) IntCal13 and Marine13 radiocarbon age calibration curves 0–50,000 years cal BP. *Radiocarbon* **55**, 1869–1887.
- Routh J., Hugelius G., Kuhry P., Filley T., Tillman P. K., Becher M. and Crill P. (2014) Multi-proxy study of soil organic matter dynamics in permafrost peat deposits reveal vulnerability to climate change in the European Russian Arctic. *Chem. Geol.* **368**, 104–117.
- Russell J. M., Hopmans E. C., Loomis S. E., Liang J., Sinnighe and Damsté J. S. (2018) Distributions of 5- and 6-methyl branched glycerol dialkyl glycerol tetraethers (brGDGTs) in East African lake sediment: effects of temperature, pH, and new lacustrine paleotemperature calibrations. *Org. Geochem.* **117**, 56–69.
- Salmon V. G., Schädel C., Bracho R., Pegoraro E., Celis G., Mauritz M., Mack M. C. and Schuur E. A. G. (2018) Adding depth to our understanding of nitrogen dynamics in permafrost soils. *J. Geophys. Res. Biogeosci.* **123**, 2497–2512.
- Santos G. M. and Ormsby K. (2013) Behavioral variability in ABA chemical pretreatment close to the 14C age limit. *Radiocarbon* **55**, 534–544.
- Schädel C., Schuur E. a. G., Bracho R., Elberling B., Knoblauch C., Lee H., Luo Y., Shaver G. R. and Turetsky M. R. (2014) Circumpolar assessment of permafrost C quality and its vulnerability over time using long-term incubation data. *Glob. Chang. Biol.* **20**, 641–652.

- Scheffer M., Hirota M., Holmgren M., Van Nes E. H. and Chapin F. S. (2012) Thresholds for boreal biome transitions. *Proc. Natl. Acad. Sci.* **109**, 21384–21389.
- Schimel J. P. and Chapin F. S. (1996) Tundra plant uptake of amino acid and  $\text{NH}_4 +$  nitrogen in situ: plants complete well for amino acid N. *Ecology* **77**, 2142–2147.
- Schirrmeyer L., Froese D., Tumskey V., Wetterich S., Grosse G. and Wetterich S. (2013) Yedoma: late pleistocene ice-rich syngenetic permafrost of Beringia. *Encycl. Quat. Sci.* **3**, 542–552.
- Schirrmeyer L., Kunitzky V., Grosse G., Wetterich S., Meyer H., Schwamborn G., Babiy O., Derevyagin A. and Siegert C. (2011) Sedimentary characteristics and origin of the Late Pleistocene Ice Complex on north-east Siberian Arctic coastal lowlands and islands – a review. *Quat. Int.* **241**, 3–25.
- Schirrmeyer L., Meyer H., Andreev A., Wetterich S., Kienast F., Bobrov A., Fuchs M., Sierralta M. and Herzschuh U. (2016) Late Quaternary paleoenvironmental records from the Chatanika River valley near Fairbanks (Alaska). *Quat. Sci. Rev.* **147**, 259–278.
- Schirrmeyer L., Siegert C., Kunitzky V. V., Grootes P. M. and Erlenkeuser H. (2002) Late quaternary ice-rich permafrost sequences as a paleoenvironmental archive for the Laptev Sea Region in Northern Siberia. *Int. J. Earth Sci.* **91**, 154–167.
- Schmidt M. W. I., Knicker H. and Kögel-Knabner I. (2000) Organic matter accumulating in Aeh and Bh horizons of a Podzol – chemical characterization in primary organo-mineral associations. *Org. Geochem.* **31**, 727–734.
- Schuur E. A. G., Crummer K. G., Vogel J. G. and Mack M. C. (2007) Plant species composition and productivity following permafrost thaw and thermokarst in Alaskan tundra. *Ecosystems* **10**, 280–292.
- Schuur E. A. G., McGuire A. D., Grosse G., Harden J. W., Hayes D. J., Hugelius G., Koven C. D. and Kuhry P. (2015) Climate change and the permafrost carbon feedback. *Nature* **520**, 171–179.
- Schuur E. A. G., Vogel J. G., Crummer K. G., Lee H., Sickman J. O. and Osterkamp T. E. (2009) The effect of permafrost thaw on old carbon release and net carbon exchange from tundra. *Nature* **459**, 556–559.
- Schuur E., Bockheim J. and Canadell J. (2008) Vulnerability of permafrost carbon to climate change: implications for the global carbon cycle. *Bioscience*.
- Shanahan T. M., Hughen K. a. and Van Mooy B. A. S. (2013) Temperature sensitivity of branched and isoprenoid GDGTs in Arctic lakes. *Org. Geochem.* **64**, 119–128.
- Shields M. R., Bianchi T. S., Gélinas Y., Allison M. A. and Twilley R. R. (2016) Enhanced terrestrial carbon preservation promoted by reactive iron in deltaic sediments. *Geophys. Res. Lett.* **43**, 1149–1157.
- Shur Y., Hinkel K. M. and Nelson F. E. (2005) The transient layer: Implications for geocryology and climate-change science. *Permafrost. Periglac. Process.* **16**, 5–17.
- Spencer R. G. M., Aiken G. R., Dyda R. Y., Butler K. D., Bergamaschi B. A. and Hernes P. J. (2010) Comparison of XAD with other dissolved lignin isolation techniques and a compilation of analytical improvements for the analysis of lignin in aquatic settings. *Org. Geochem.* **41**, 445–453.
- Stapel J. G., Schirrmeyer L., Overduin P. P., Wetterich S., Strauss J., Horsfield B. and Mangelsdorf K. (2016) Microbial lipid signatures and substrate potential of organic matter in permafrost deposits: Implications for future greenhouse gas production. *J. Geophys. Res. Biogeosci.* **121**, 2652–2666.
- Stapel J. G., Schwamborn G., Schirrmeyer L., Horsfield B. and Mangelsdorf K. (2018) Substrate potential of last interglacial to Holocene permafrost organic matter for future microbial greenhouse gas production. *Biogeosciences* **15**, 1969–1985.
- Strauss J., Schirrmeyer L., Grosse G., Fortier D., Hugelius G., Knoblauch C., Romanovsky V., Schädel C., Schneider von Deimling T., Schuur E. A. G., Shmelev D., Ulrich M. and Veremeeva A. (2017) Deep Yedoma permafrost: a synthesis of depositional characteristics and carbon vulnerability. *Earth-Sci. Rev.* **172**, 75–86.
- Strauss J., Schirrmeyer L., Grosse G., Wetterich S., Ulrich M., Herzschuh U. and Hubberten H.-W. (2013) The deep permafrost carbon pool of the Yedoma region in Siberia and Alaska. *Geophys. Res. Lett.* **40**, 6165–6170.
- Strauss J., Schirrmeyer L., Mangelsdorf K., Eichhorn L., Wetterich S. and Herzschuh U. (2015) Organic-matter quality of deep permafrost carbon – A study from Arctic Siberia. *Biogeosciences* **12**, 2227–2245.
- Thevenot M., Dignac M.-F. F. and Rumpel C. (2010) Fate of lignins in soils: a review. *Soil Biol. Biochem.* **42**, 1200–1211.
- Vandenberghe J., French H. M., Gorbunov A., Marchenko S., Velichko A. A., Jin H., Cui Z., Zhang T. and Wan X. (2014) The Last Permafrost Maximum (LPM) map of the northern hemisphere: permafrost extent and mean annual air temperatures, 25–17 ka BP. *Boreas* **43**, 652–666.
- Vogel J. S., Nelson D. E. and Southon J. R. (1987) 14C background levels in an accelerator mass spectrometry system. *Radiocarbon* **29**, 323–333.
- Vogel J., Schuur E. A. G., Trucco C. and Lee H. (2009) Response of CO<sub>2</sub> exchange in a tussock tundra ecosystem to permafrost thaw and thermokarst development. *J. Geophys. Res. Biogeosci.* **114**(G04018), 1–14.
- Vonk J. E., Mann P. J., Davydov S., Davydova A., Spencer R. G. M., Schade J., Sobczak W. V., Zimov N., Zimov S., Bulygina E., Eglinton T. I. and Holmes R. M. (2013) High biolability of ancient permafrost carbon upon thaw. *Geophys. Res. Lett.* **40**, 2689–2693.
- Weijers J. W., Schouten S., van den Donker J. C., Hopmans E. C., Sinnighe and Damsté J. S. (2007) Environmental controls on bacterial tetraether membrane lipid distribution in soils. *Geochim. Cosmochim. Acta* **71**, 703–713.
- Weiss N., Blok D., Elberling B., Hugelius G., Jørgensen C. J., Siewert M. B. and Kuhry P. (2016) Thermokarst dynamics and soil organic matter characteristics controlling initial carbon release from permafrost soils in the Siberian Yedoma region. *Sed. Geol.* **340**, 38–48.
- Wetterich S., Rudaya N., Tumskey V., Andreev A. a., Opel T., Schirrmeyer L. and Meyer H. (2011) Last Glacial Maximum records in permafrost of the East Siberian Arctic. *Quat. Sci. Rev.* **30**, 3139–3151.
- Wetterich S., Tumskey V., Rudaya N., Andreev A. A., Opel T., Meyer H., Schirrmeyer L. and Hüls M. (2014) Ice Complex formation in arctic East Siberia during the MIS3 Interstadial. *Quat. Sci. Rev.* **84**, 39–55.
- Wooller M. J., Zazula G. D., Blinnikov M., Gaglioti B. V., Bigelow N. H., Sanborn P., Kuzmina S. and La Farge C. (2011) The detailed palaeoecology of a mid-Wisconsinan interstadial (ca. 32 00014C a BP) vegetation surface from Interior Alaska. *J. Quat. Sci.* **26**, 746–756.
- Xu X., Trumbore S. E., Zheng S., Southon J. R., McDuffee K. E., Luttgen M. and Liu J. C. (2007) Modifying a sealed tube zinc reduction method for preparation of AMS graphite targets: reducing background and attaining high precision. *Nucl. Instrum. Methods Phys. Res. Sect. B Beam Interact. Mater. Atoms* **259**, 320–329.
- Zech M., Andreev A., Zech R., Müller S., Hambach U., Frechen M. and Zech W. (2010) Quaternary vegetation changes derived from a loess-like permafrost palaeosol sequence in northeast Siberia using alkane biomarker and pollen analyses. *Boreas* **4**, 540–550.

- Zhang X., Bianchi T. S., Cui X., Rosenheim B. E., Ping C. L., Hanna A. J. M., Kanevskiy M., Schreiner K. M. and Allison M. A. (2017) Permafrost organic carbon mobilization from the watershed to the Colville River Delta: evidence from  $^{14}\text{C}$  ramped pyrolysis and lignin biomarkers. *Geophys. Res. Lett.* **44**, 1–10.
- Zimov N. S., Zimov S. a., Zimova A. E., Zimova G. M., Chuprynin V. I. and Chapin F. S. (2009) Carbon storage in permafrost and soils of the mammoth tundra-steppe biome: role in the global carbon budget. *Geophys. Res. Lett.* **36** (L02502), 1–6.
- Zimov S. A., Davydov S. P., Zimova G. M., Davydova A. I., Schuur E. A. G., Dutta K. and Chapin F. S. (2006) Permafrost carbon: stock and decomposability of a globally significant carbon pool. *Geophys. Res. Lett.* **33**, L20502.

*Associate editor:* Ann Pearson